

International Journal of Modern Physics A
© World Scientific Publishing Company

A comprehensive model of soft interactions in the LHC era

Errol Gotsman

*Department of Particle Physics, School of Physics and Astronomy, Raymond and Beverly
Sackler Faculty of Exact Science, Tel Aviv University, Tel Aviv, 69978, Israel
gotsman@post.tau.ac.il*

Eugene Levin

*Department of Particle Physics, School of Physics and Astronomy, Raymond and Beverly
Sackler Faculty of Exact Science, Tel Aviv University, Tel Aviv, 69978, Israel
Departamento de Física, Universidad Técnica Federico Santa María, Avda. España 1680
and Centro Científico-Tecnológico de Valparaíso, Casilla 110-V, Valparaíso, Chile
leving@post.tau.ac.il, eugeniy.levin@usm.cl*

Uri Maor

*Department of Particle Physics, School of Physics and Astronomy, Raymond and Beverly
Sackler Faculty of Exact Science, Tel Aviv University, Tel Aviv, 69978, Israel
maor@post.tau.ac.il*

*Contribution to appear in the special issue of the International Journal of Modern Physics A
on "Elastic and Diffractive Scattering", coordinated by Christophe Royon*

TAUP 2981/14

In this review we present our model which is an example of the self consistent approach that incorporates our theoretical understanding of long distance physics, based both on N=4 SYM for strong coupling and on the matching with the perturbative QCD approach. We demonstrate how important and decisive the LHC data were on strong interactions which led us to a set of the phenomenological parameters that fully confirmed our theoretical expectations, and produced a new picture of the strong interaction at high energy. We also show how far we have come towards creating a framework for the description of minimal bias events for high energy scattering without generating Monte Carlo codes.

Keywords: N=4 SYM; Perturbative QCD, Models for soft interaction, Pomeron calculus; diffraction and inclusive production.

PACS numbers: 13.85.-t, 13.85.-Hd, 11.55=m, 11.55 Bg

1. Introduction

The LHC data¹⁻⁴ changed our understanding of soft interactions at high energy. Regrettably, none of the phenomenological models based on the Reggeon approach⁵⁻⁹

were successful in predicting this data, in spite of having a large number of fitted parameters. This fact is not surprising since quantum chromodynamics (QCD), which is a microscopic theory, has a theoretical problem, i.e. accounting for the confinement of quarks and gluons. There is a wide spread belief that the confinement of quarks and gluons is not a fundamental problem, this is based on the fact that lattice QCD shows that such a phenomenon exists and can be calculated. Soft interactions at high energy, provides us with an excellent example of processes in which the lattice approach fails to produce any framework which incorporates a satisfactory description of the experimental data. Even though confinement is a difficult fundamental problem, we firmly believe that soft interaction data, as well as its interpretation in the framework of a model approach, will lead to a deeper understanding of the origin of confinement and its properties.

To comprehend how much the LHC data contribute to our understanding of high energy soft processes, we compare the general characterizations of these processes before and after the LHC.

- Before LHC: At the time, Donnachie and Landshoff (DL) provided a good description¹² of the total and elastic cross sections in the ISR-Tevatron energy range. The DL model has a severe flaw since it does not include the effect of shadowing/screening corrections on the Pomeron and the secondary Reggeons exchange amplitudes. This approximation is valid, though, in the calculation of the elastic hadronic amplitudes below the LHC energy.⁵ However, it fails to describe the diffractive channels in which unitarity screening are significant at energies as low as the ISR.

The DL Pomeron trajectory is:

$$\alpha_P = 1 + \Delta_P + \alpha'_P t = 1 + 0.08 \div 0.13 + 0.25 t, \quad (1.1)$$

where t is the square of the transferred momentum of the Pomeron and the slope α'_P is measured in GeV^{-2} . Both Pomeron and secondary Reggeons stem from a natural generalization of QCD string theory.¹³ Therefore, this simple phenomenology, together with the string approach, provides a self consistent and beautiful picture of soft interactions at high energies. As noted, the simple DL phenomenology of a single Pomeron exchange cannot reproduce the diffractive sector, which follows directly from the wave nature of the colliding particles. However, we have a small parameter: the ratio $R = \frac{1}{2}\sigma_{sd}/\sigma_{el} \approx 0.18$ at the Tevatron energies. Hence, we can develop a perturbative approach with respect to this parameter. The partial single Pomeron exchange elastic amplitude at fixed impact parameters (b) is:

$$A_P(b) = g_1 g_2 \int d^2 b' S_1(\vec{b} - \vec{b}') S_2(\vec{b}') e^{\Delta_{pom} Y - \frac{b^2}{4\alpha'_P Y}} < 1. \quad (1.2)$$

In Eq. (1.2) g_i is the vertex of the Pomeron interaction with the hadrons, $S_i(b_i)$ is the profile function at this vertex and $Y = \ln s$. One can see from

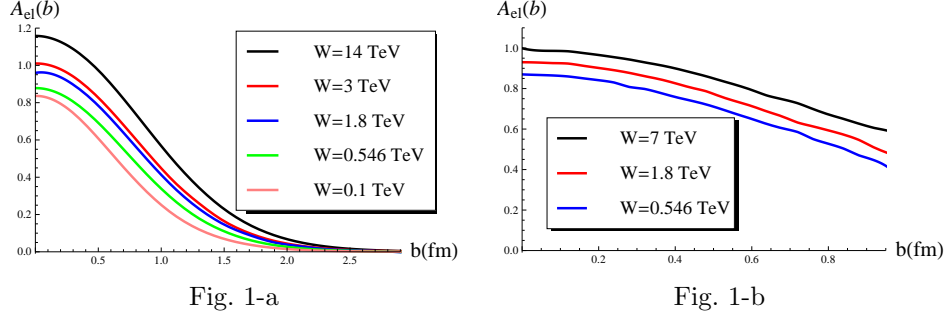


Fig. 1. The elastic amplitude calculated, using Donnachie-Landshoff Pomeron of Eq. (1.1) (Fig. 1-a) and using the data on elastic cross section (Fig. 1-b) $A_{el}(b) = \int \frac{q_{\perp} q_{\perp}}{4\pi} \sqrt{\frac{d\sigma_{el}(s, t = -q_{\perp}^2)}{dt}} \frac{16\pi}{(1+\rho)} J_0(q_{\perp} b)$. For Fig. 1-b the curves are taken from Ref.¹⁰

Fig. 1, which illustrates Eq. (1.2), that $A_P(b)$ reaches 1 at the Tevatron energy and, therefore, one expects that the DL model will need to be amended for the LHC range of energies. The second weakness of this simple model is that the small parameter is under estimated, as we also need to add the double diffraction cross section, $(R = (\frac{1}{2}\sigma_{sd} + \sigma_{dd}) / \sigma_{el} \approx 0.4 \div 0.5$ in spite of the large σ_{dd} errors.)

- Post LHC: Substantial shadowing corrections need to be taken into account to describe the LHC data. In models, based on Pomerons and their interactions, the Pomeron trajectory emerges as

$$\alpha_P = 1 + \Delta_P + \alpha'_P t = 1 + (0.2 \div 0.3) + (\alpha'_P < 0.02) t, \quad (1.3)$$

which cannot be obtained from a string model approach. On the other hand, such a Pomeron provides a natural matching with perturbative QCD (pQCD),^{14,15} and N=4 SYM theory.¹⁶⁻¹⁹

The goal of this review is to discuss two main topics: why and how such a Pomeron can be expected both from theoretical approaches, and from the description of the LHC experimental data; and the progress we have made in our attempts to build a model that is able to describe the structure of the bias events without relying on Monte Carlo codes.

As we lack a solid theoretical basis in non perturbative QCD to build a model, we need to make an educated guess as to which theoretical approach we should employ. Our choice will be discussed in the next section which, on its own, is a review of useful theoretical ideas regarding the strong interactions. In the third section we present the key assumptions and the main formulae of our model. In section 4 we discuss the qualitative features of the model.

4 *E. Gotsman, E. Levin and U. Maor*

2. Theoretical background

2.1. General theorems

As the methods of non-perturbative QCD are in an embryonic stage, we rely on the consequences of the general features of the scattering amplitude, i.e. analyticity, crossing symmetry and unitarity.

2.1.1. Unitarity

To formulate the unitarity constraints, we introduce a complete set of orthogonal functions $\{\psi_i\}$ which diagonalize the interaction matrix \mathbf{T}

$$A_{i,k}^{i'k'} = \langle \psi_i | \psi_k | \mathbf{T} | \psi_{i'} | \psi_{k'} \rangle = A_{i,k} \delta_{i,i'} \delta_{k,k'}. \quad (2.4)$$

In this representation the hadron wave function can be written as

$$\psi_h = \sum_i c_i^h \psi_i \quad (2.5)$$

The unitarity constraints have the form

$$2 \operatorname{Im} A_{i,k}(s, b) = |A_{i,k}(s, b)|^2 + G_{i,k}^{in}(s, b), \quad (2.6)$$

where $G_{i,k}^{in}$ denote the contribution of all non diffractive inelastic processes, i.e. it is the summed probability for these final states to be produced in the scattering of a state i off state k . In Eq. (2.6) $\sqrt{s} = W$ is the energy of the colliding hadrons and b denotes the impact parameter. A simple solution to Eq. (2.6) at high energies has the eikonal form with an arbitrary opacity Ω_{ik} , where the real part of the amplitude is much smaller than the imaginary part.

$$A_{i,k}(s, b) = i \left(1 - \exp \left(-\frac{\Omega_{i,k}(s, b)}{2} \right) \right), \quad (2.7)$$

$$G_{i,k}^{in}(s, b) = 1 - \exp(-\Omega_{i,k}(s, b)). \quad (2.8)$$

Eq. (2.8) implies that the probability that the initial projectiles (i, k) will reach the final state interaction unchanged, regardless of the initial state re-scatterings, is given by $P_{i,k}^S = \exp(-\Omega_{i,k}(s, b))$.

Integrating Eq. (2.6) over b we have

$$2 \operatorname{Im} A_{i,k}(s, t=0) = 2 \int d^2b \operatorname{Im} A_{i,k}(s, b) = \sigma_{el} + \sigma_{in} = \sigma_{tot}. \quad (2.9)$$

Which is the optical theorem.

2.1.2. The unitarity bound

Using two inputs: the unitarity constraints and the behaviour of the amplitude at large b , we derive a bound on the total cross section.²⁰ Indeed, from Eq. (2.6) $A_{ik} \leq 1$. The fact that we have the lightest hadron (pion) with mass m_π , implies that

the amplitude decreases as $\exp(-2m_\pi b)$. We can re-write Eq. (2.9) and Eq. (2.6) in the form

$$\sigma_{tot} = 2 \int d^2b \operatorname{Im} A_{i,k}(s, b) \leq 2 \int^{b^*} d^2b + 2 \int_{b^*} d^2b A_{i,k}(s, b \rightarrow \infty), \quad (2.10)$$

where b^* can be determined from the amplitude at large b , in which we assume that $A_{i,k}(s, b \rightarrow \infty) = Cs^\Delta \exp(-2m_\pi b)$. The equation for b^* has the form

$$A_{i,k}(s, b \rightarrow \infty) = Cs^\Delta \exp(-2m_\pi b^*) = 1, \quad \text{with a solution } b^* = \frac{\Delta}{2m_\pi} \ln s. \quad (2.11)$$

Using Eq. (2.11), we obtain from Eq. (2.10) that

$$\sigma_{tot} \leq 4\pi \left(\frac{\Delta}{2m_\pi} \ln s \right)^2 = \text{Const } \ln^2 s. \quad (2.12)$$

2.1.3. Good-Walker mechanism

We have eluded to the fact that the processes of diffraction dissociation play an important role in the description of high energy scattering. Indeed, in the framework of the Pomeron approach, they provide a qualitative measure of the contribution of the shadowing correction. The origin of diffraction lies in the wave nature of the scattering particles and can be illustrated in the following way: In the initial state we have the wave function of two non-interacting hadrons

$$\Psi_{in} = \psi_{h_1} \psi_{h_2} = \left(\sum_i c_i^{h_1} \psi_i \right) \left(\sum_k c_k^{h_2} \psi_k \right), \quad (2.13)$$

while the wave function of the final state has the form

$$\Psi_{fin} = \mathbf{T} \Psi_{in} = \sum_{i,k} A_{ik} c_i^{h_1} c_k^{h_2} \psi_i \psi_k \neq \psi_{h_1} \psi_{h_2}. \quad (2.14)$$

Generally, the final state is not the same as the initial state. Only if $\psi_h = \psi_k$, does the interaction lead to the case where the two hadrons in the final state are identical to the two hadrons in the initial state. Therefore, the interaction results in a cross section which is proportional to $\left| \langle \Psi_{fin} | \mathbf{T} | \Psi_{in} \rangle \right|^2$, which can be re-written in the form

$$\left| \langle \Psi_{fin} | \mathbf{T} | \Psi_{in} \rangle \right|^2 = \sum_{i,k} A_{ik}^2 \left(c_i^{h_1} \right)^2 \left(c_k^{h_2} \right)^2 = \langle \psi_{h_1} \psi_{h_2} | \mathbf{T}^2 | \psi_{h_1} \psi_{h_2} \rangle. \quad (2.15)$$

The elastic cross section is proportional to $\left| \langle \Psi_{in} | \mathbf{T} | \Psi_{in} \rangle \right|^2 = \left| \langle \psi_{h_1} \psi_{h_2} | \mathbf{T} | \psi_{h_1} \psi_{h_2} \rangle \right|^2$. Finally,

$$\sigma_{diff} \propto \langle \psi_{h_1} \psi_{h_2} | \mathbf{T}^2 | \psi_{h_1} \psi_{h_2} \rangle - \left| \langle \psi_{h_1} \psi_{h_2} | \mathbf{T} | \psi_{h_1} \psi_{h_2} \rangle \right|^2. \quad (2.16)$$

These ideas on the origin of diffraction were introduced in the early 50's by Landau, Pomeranchuk, Feinberg, Ahiezer, Ter-Mikaelyan and Sitenko (see the review by Feinberg and Pomeranchuk²¹) and were crystallized and put into an elegant theoretical framework by Good and Walker.²²

2.2. Reggeon approach

For more than five decades the Reggeon approach has provided the main tool for high energy scattering phenomenology. This approach connects the existence of resonances with the asymptotic behaviour of high energy scattering (see Refs.^{23–25}). When considering the exchange of a resonance with a spin j , one has to also include all excitation with spin $j + 2, j + 4, \dots$ (keeping all other quantum numbers unchanged). These particles lie on a Regge trajectory $\alpha_R(t)$ with $\alpha_R(t = M_j^2) = j$. The contribution to the scattering amplitude initiated by the exchange of all resonances can be described as an exchange of the new object: the Reggeon, and its contribution to the scattering amplitude is given by a simple function:

$$A_R(s, t) = g_p(m_1, M_1, t) g_t(m_2, M_2, t) \cdot R(s, t) \quad (2.17)$$

$$\text{with a Reggeon propagator } R(s, t) = \frac{\left(\frac{s}{s_0}\right)^{\alpha_R(t)} \pm \left(-\frac{s}{s_0}\right)^{\alpha_R(t)}}{\sin \pi \alpha_R(t)} \equiv \eta(t) \left(\frac{s}{s_0}\right)^{\alpha_R(t)}$$

$\alpha_R(t)$ is a function of the momentum transfer which we call the Reggeon trajectory. Eq. (2.17) reflects the factorization property of the Reggeon: the dependence on mass of the interacting hadrons is concentrated in the vertices $g_p(m_i, M_i, t)$ and $g_t(m_2, M_2, t)$, while the Reggeon propagator depends only on s and t . The functions $g_{p,t}(m_i, M_i, t)$ are phenomenological functions that describe the vertex of the Reggeon interaction with hadrons with masses m_i and M_i . In the region of positive t the zeros of $\sin \pi \alpha_R(t)$ generate the resonances with a mass M_j at $\alpha_R(t = M_j^2) = j$. The factor $\eta(t)$ depends only on the Reggeon trajectory and determines the phase of the amplitude.

The name of the new object, as well as the form of the amplitude, came from analysing the properties of the scattering amplitude in the t channel, using the angular momentum representation.²³

Among the Reggeons which correspond to the measured spectrum of their corresponding resonances, there is one Reggeon which does not have a resonance on its trajectory. Its existence was assumed to be able to describe the behaviour of the total cross section. This special Reggeon is called the Pomeron, and it has an intercept which is close to unity, as the energy behaviour of the total cross section does not display a decrease with increasing energy. Since $\alpha_P(0) \rightarrow 1$ the exchange of the Pomeron leads to a mostly imaginary amplitude, and it generates processes of multiparticle production.

The s -channel structure of the Pomeron has a simple explanation in the framework of the parton picture^{26–28} which are summarized in the two pictures of Fig. 3.

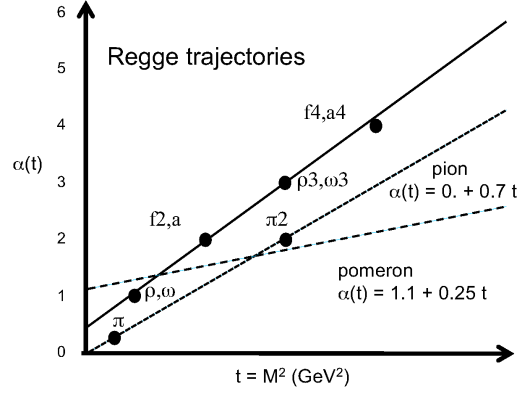


Fig. 2. The typical examples of the Reggeon trajectory with resonances at $t > 0$ ¹² adapted from Ref.¹¹ The dotted line in the right figure shows the DL Pomeron.

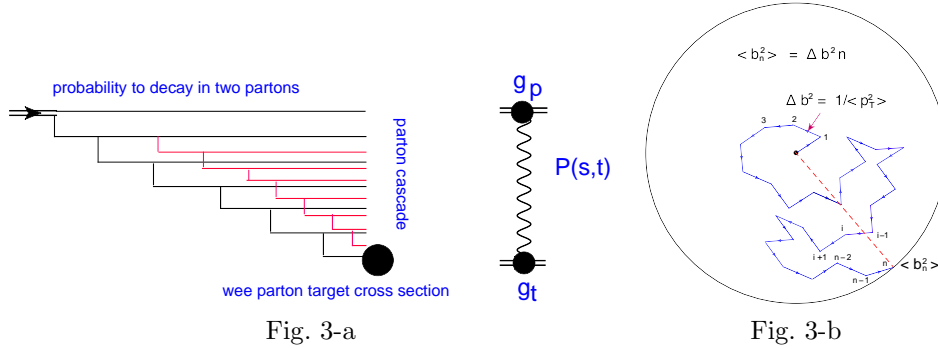


Fig. 3-a

Fig. 3-b

Fig. 3. The parton approach to high energy scattering: longitudinal structure of the parton cascade (Fig. 3-a) and Gribov's diffusion (Fig. 3-b).

Fig. 3-a states that the total cross section induced by a single Pomeron exchange is equal to

$$\sigma = \sum_{n=2}^{\infty} \int_0^Y dy_1 \int_0^{y_1} dy_2 \dots \int_0^{y_{n-1}} dy_n \prod_{i=2}^{n-1} d^2 p_{i,T} \Psi^* (\{x_i, \vec{p}_{i,T}\}, y_n, \vec{p}_{n,T}) \Psi (\{x_i, \vec{p}_{i,T}\}, \vec{p}_{n,T}) \sigma_{\text{parton}} (y_n, p_{n,T}), \quad (2.18)$$

where Ψ is the wave function of the partons (point-like particles) which have restricted transverse momentum $p_{i,T} \leq \mu$. μ does not depend on the total energy. We assume that the partons are distributed uniformly in the rapidity range $(0, Y)$ and the integral over dy_n converges.

Fig. 3-b illustrates Gribov's diffusion picture in the transverse plane of the partons populating the parton cascade. It is based on the uncertainty principle in which $\Delta b p_{i,T} \sim 1$ for the emission of a parton in the cascade. This figure

8 *E. Gotsman, E. Levin and U. Maor*

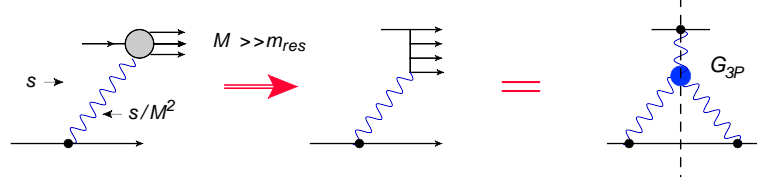


Fig. 4. The parton approach to high energy scattering: processes of diffraction production of large mass. Wavy lines denote Pomerons. The blob shows the triple Pomeron vertex.

shows that after n -emissions the partons are distributed in the area with a radius $b_n^2 = (1/\langle p_{i,T} \rangle^2) n$. Since $n \propto Y$ we get $R^2 \propto (1/\langle p_{i,T} \rangle^2) Y = \alpha'_P Y$.

In the parton approach the processes of diffraction dissociation at large mass ($M > m_{res}$ where m_{res} is the mass of the resonances) is closely related to the interaction of the Pomerons, see Fig. 4. It could be described by the following expression

$$\frac{M^2 d\sigma_{diff}^{3P}}{dM^2} = 2 \int dt g_p(t=0) g_t^2(t) G_{3P}(t) \text{Im}P(M^2, t=0) P\left(\frac{s}{M^2}, t\right) P^*\left(\frac{s}{M^2}, t\right). \quad (2.19)$$

If $\Delta_P = 0$, this contribution corresponds to a diffractive channel, which is not included in the GW mechanism. Averaging Eq. (2.15) leads to a divergent series. However, in the case of $\Delta_P > 0$, the integral of Eq. (2.19) over M is convergent, and this contribution is a part, of the GW mechanism.²⁹ Fig. 4 shows an example of a triple Pomeron interaction.

Our knowledge of the Pomeron interaction was summarized in Gribov Pomeron calculus,³⁰ which can be formulated by the following path integral:

$$\begin{aligned} Z[\Phi, \Phi^+] &= \int D\Phi D\Phi^+ e^S \text{ with } S = S_0 + S_I + S_E \\ , S_0 &= \int dY d^2b \Phi^+(Y, b) \left\{ -\frac{d}{dY} + \Delta + \alpha'_P \nabla^2 \right\} \Phi(Y, b); \\ S_I &= G_{3P} \int dY d^2b \{ \Phi(Y, b) \Phi^+(Y, b) \Phi^+(Y, b) + h.c. \}. \end{aligned} \quad (2.20)$$

S_E specifies the interaction with hadrons or nuclei. $\Phi(Y, r)$ describes the Pomeron with rapidity Y and impact parameter b . It turns out that Eq. (2.20) has a simple statistical interpretation and can be re-written as an equation presenting the probability P_n to have n -Pomerons at rapidity Y . The equation has the form specified in Ref.^{31,32}

$$\begin{aligned} -\frac{\partial P_n(y, b)}{\partial y} + \alpha'_P \nabla^2 P_n(y, b) &= G_{3P} \{ -n P_n(y, b) + (n-1) P_{n-1}(y, b) \} \\ &+ G_{3P} \{ -n(n-1) P_n(y, b) + (n+1)n P_{n+1}(y, b) \}. \end{aligned} \quad (2.21)$$

The problem of the Pomeron interactions has not been completely solved, as we have failed to find theoretical arguments for restricting the number of Pomeron

interaction vertices, as well as finding the term S_E in Eq. (2.20).

2.3. Perturbative QCD

In pQCD the high energy Pomeron behaviour, arises in a natural way with an intercept $\alpha_P(0) = 1 + C\bar{\alpha}_S$,^{14,15,33} where $\bar{\alpha}_S$ is the QCD coupling. However, in spite of the power-like increase with energy, the expression for the high energy contribution to the scattering amplitude, differs significantly from the corresponding Pomeron expression. The best way to see this is to compare the QCD contribution (which is a BFKL Pomeron) with Eq. (2.17). The propagator of the BFKL Pomeron for the scattering of two dipoles with sizes r and R has the form¹⁴

$$P_P(Y, b) \implies P_{\text{BFKL}}(Y, r, R) = \frac{rR}{\sqrt{Y}} e^{\Delta_{\text{BFKL}} Y - \frac{\ln^2(r^2/R^2)}{DY}}, \quad (2.22)$$

with $\Delta_{\text{BFKL}} = 2 \ln 2 \bar{\alpha}_S$ and $D = 14\zeta(3)\bar{\alpha}_S = 16.828 \bar{\alpha}_S$.

Note that:

- (i) The BFKL Pomeron is not an angular momentum pole but a branch cut, since its Y -dependence has an additional $\ln s$ term.
- (ii) It does not depend on the impact parameter.
- (iii) The BFKL propagator depends on the sizes of dipoles, consequently, the BFKL Pomeron does not factorize..

Despite a different structure of the Pomeron in QCD, the key partonic formula of Eq. (2.18) works with $\sigma_{\text{parton}}(y_n, p_{n,T}) = \sigma_{\text{dipole-dipole}}^{BA}$, where σ^{BA} is calculated in the Born approximation of pQCD. This cross section does not depend on Y . The similarities between the QCD and the partonic cascades, leads to the same triple BFKL Pomeron mechanism for diffractive production of large masses shown in Fig. 4. The similarities between the Reggeon calculus and the interaction between BFKL Pomerons, is clearly seen in the path integral formulation of the BFKL Pomeron interaction, where, instead of Eq. (2.20), the S_0 and S_I contributions have different forms⁴¹ than in Eq. (2.20):

$$\begin{aligned} S_0 &= \int dY dY' d^2x_1 d^2x_2 d^2x'_1 d^2x'_2 \Phi^+(x_1, x_2; Y) \nabla_1^2 \nabla_2^2 \left(\frac{\partial}{\partial Y} - \mathcal{H} \right) \Phi(x'_1, x'_2; Y'); \\ S_I &= \frac{2\pi\bar{\alpha}_S^2}{N_c} \int dY' \int \frac{d^2x_1 d^2x_2 d^2x_3}{x_{12}^2 x_{23}^2 x_{13}^2} \\ &\cdot \{ (x_{12}^4 \nabla_1^2 \nabla_2^2 \Phi(x_1, x_2; Y')) \cdot \Phi^+(x_1, x_3; Y') \Phi^+(x_3, x_2; Y') + h.c. \}; \\ \mathcal{H}f(x_1, x_2; Y) &= \frac{\bar{\alpha}_S}{2\pi} \int d^2x_3 \frac{x_{12}^2}{x_{23}^2 x_{13}^2} (f(x_1, x_2; Y) - f(x_1, x_3; Y) - f(x_3, x_2; Y)). \end{aligned} \quad (2.23)$$

Comparing Eq. (2.20) and Eq. (2.23), one can see that in QCD, we have the field depending on the size of the interacting dipole. The particular expression for the triple Pomeron interaction depends on the strength of the triple Pomeron coupling, it is of the order of $\bar{\alpha}_S^2$ ($G_{3P} \propto \bar{\alpha}_S^2$). There is no Gribov's diffusion (the term $\alpha'_P \nabla_b^2$

10 *E. Gotsman, E. Levin and U. Maor*

in Eq. (2.20)). In principle, the four Pomeron interaction should appear in Eq. (2.23) but it is suppressed (see Ref.³⁴).

2.4. $N=4$ SYM

At present $N=4$ SYM is the only theory we know which can deal with a large coupling constant. Hence, we use this theory as the guide to handle physics phenomena in this regime. The attractive feature of this theory is that $N=4$ SYM with small coupling, leads to normal QCD-like physics (see Refs.^{17,18}) with OPE and linear equations for DIS, as well as the BFKL equation for the high energy amplitude. The high energy amplitude reaches the unitarity limit: black disc regime, in which half of the cross section is due to elastic scattering, and half is associated with processes of multiparticle production.

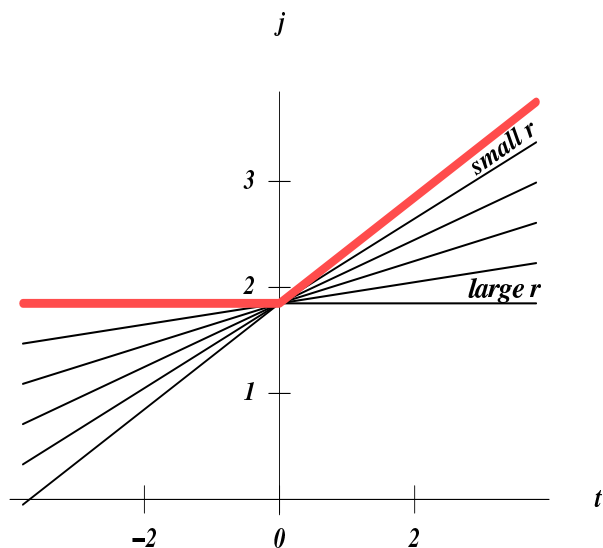


Fig. 5. The behaviour of the Pomeron trajectory in $N=4$ SYM according to Ref.¹⁹ The figure is taken from Ref.¹⁹

This theory has an analytical solution due to AdS/CFT correspondence, and can be reduced to weak gravity in AdS_5 space.

In the strong coupling limit, the following are the main features of this theory:^{19,37–40}

- (i) It has a soft Pomeron which, in this case, is the reggeized graviton with a large intercept $\alpha(0)_P = 2 - 2/\sqrt{\lambda}$, where, $\lambda = 4\pi N_c \alpha_S^{YM}$. α_S^{YM} is the QCD-like coupling;
- (ii) The main contribution to the total cross section at high energy is due to the processes of elastic scattering and diffractive dissociation;
- (iii) The leading Pomeron trajectory has a form shown in Fig. 5. Namely, a Regge pole with $\alpha'_P = 0$ in the scattering region ($t < 0$), while $\alpha'_P > 0$ in the resonance

region of positive t ;

(iv) The Pomerons (gravitons) interact with the triple Pomeron vertex which is small ($\propto 2/\sqrt{\lambda}$);

(v) The only source of diffraction production is the GW mechanism in which the fifth coordinate z plays a role of the degree of freedom. At first sight the small value of $\alpha'_{\mathcal{P}}$ is not related to the small size of the partons in this theory. It is related to the small values of the fifth coordinate r (see Fig. 5). The physical meaning of this coordinate is the typical size of the colliding particles. It should be stressed that all these features appear in the theory and therefore, for the first time, we have a theoretical justification for the Reggeon-type phenomenology for high energy scattering.

To summarize, our intent is to consider the Pomeron in N=4 SYM, which is based on the discovery that, actually, it is a BFKL Pomeron. The following glossary aims to translate QCD to this theory.

Glossary		\equiv		AdS-CFT correspondence:	
N=4 SYM				QCD	
Reggeized graviton	\Longleftrightarrow			BFKL Pomeron	
z	\Longleftrightarrow			r (dipole size)	
$1 - 2/\sqrt{\lambda}$	\Longleftrightarrow			Δ_{BFKL} (intercept of the BFKL Pomeron)	
$2/\sqrt{\lambda}$	\Longleftrightarrow			D_{BFKL} (see Eq. (2.22))	

3. General features of our model

3.1. Main assumptions and parameters of our model

We have built our model using the main characteristic features of N=4 SYM and QCD approaches. We assume:

- *The Pomeron is a Regge pole.* This assumption is made so as to simplify our calculations, as we need an approach which is convenient to determine our parameters.
- $\Delta_{\mathcal{P}}$ is large ($0.2 \div 0.3$). As we have discussed, the intercept of our Pomeron turns out to be large, both in N=4 SYM and in pQCD. The range of the values for $\Delta_{\mathcal{P}}$ is taken from a fit of deep inelastic HERA data in the framework of N=4 SYM.⁴²
- The fact that we are successful in describing the experimental data with an input BFKL-like ("hard") Pomeron, means that as a result of screening corrections our "hard" Pomeron transmutes into a "soft" Pomeron, with a small effective $\Delta_{\text{eff}(\mathcal{P})} \approx 0.1$. In other words, our input Pomeron which is BFKL-like ("hard"), due to screening corrections, behaves like a "soft" Pomeron.
- $\alpha'_{\mathcal{P}} = 0$. This constraint stems both from N=4 SYM and pQCD. We have checked that the data, including the LHC output, imposes a very small value $\alpha'_{\mathcal{P}} \leq 0.028 \text{ GeV}^{-2}$ (see below).

- *Large GW components.* Large GW components occur naturally in N=4 SYM, in which this mechanism is the only source of the diffractive production. For the sake of simplicity we replace the rich structure of the produced states by one wave function, and develop a two channel model to describe the GW mechanism.
- *Only G_{3P} .* In QCD, the triple BFKL Pomeron vertex is small ($\propto \bar{\alpha}_S^2$), and the vertices for more than three Pomeron interactions contain an additional suppression. We restrict ourselves, and consider only G_{3P} coupling, so as to provide a natural matching with the QCD approach of Eq. (2.23).
- *G_{3P} is small.* In QCD, $G_{3P} \propto \alpha_S^2$ while in N=4 SYM $G_{3P} \ll 2/\sqrt{\lambda}$.

3.2. The Lagrangian of the model

3.2.1. S_0 and S_I

Using the above assumptions in terms of a functional integral we get:

$$Z[\Phi, \Phi^+] = \int D\Phi D\Phi^+ e^S \text{ with } S = S_0 + S_I + S_E, \quad (3.24)$$

where,

$$S_0 = \int dY \Phi^+(Y) \left\{ -\frac{d}{dY} + \Delta_P \right\} \Phi(Y) \quad (3.25)$$

describes the free Pomeron trajectory with an intercept Δ_P and a slope $\alpha'_P = 0$. These two features that occur both in N=4 SYM and QCD, have been included in Eq. (3.25).

S_I characterizes the interaction between Pomerons and has the form:

$$S_I = G_{3P} \int dY \left\{ \Phi(Y) \Phi^+(Y) \Phi^+(Y) + h.c. \right\}. \quad (3.26)$$

Note that we only take into account the triple Pomeron interaction. This form provides a natural matching with the pQCD approach,⁴³ and with the BFKL Pomeron calculus (see Eq. (2.23)).⁴¹ We will specify S_E which is responsible for the interaction of the target and colliding projectile, in two processes: proton-proton and proton-nucleus interactions.

Reggeon Field Theory with the action given by Eq. (3.25) and Eq. (3.26) has been solved for arbitrary S_E (see Refs.^{44,45}). This theory leads to a total cross section that decreases at ultra high energies. Thus it is necessary to include the four Pomeron vertex to prevent this decrease.⁴⁶ We will show below that this decrease occurs at ultra high energies, and we will specify the range of energies for which our model is trustworthy.

3.2.2. S_E for hadron-hadron collisions

We need to incorporate in our procedure a sufficiently large GW²² component which is required so as to describe low mass diffraction, and which follows from the N=4

SYM approach.¹⁹ We develop a two channel model which takes into account the GW mechanism, and in which the observed physical hadronic and diffractive states are written in the form

$$\psi_h = \alpha \Psi_1 + \beta \Psi_2; \quad \psi_D = -\beta \Psi_1 + \alpha \Psi_2, \quad (3.27)$$

where, $\alpha^2 + \beta^2 = 1$. Note that GW diffraction is presented by a single wave function ψ_D . The wave functions Ψ_1 and Ψ_2 diagonalize the interaction matrix (see Eq. (2.4) with $i, k = 1, 2$). Bearing in mind Eq. (3.27), we can write S_E in the form

$$S_E = - \int dY' d^2b \sum_{i=1}^2 \left\{ \Phi(Y') g^{(i)}(b) \delta(Y' - 0) + \Phi(Y') g^{(i)}(b) \delta(Y - Y') \right\}. \quad (3.28)$$

$g^{(i)}$ denotes the vertex of the Pomeron interaction with the state i . This is described by either the wave functions Ψ_1 or Ψ_2 . $Y' = 0$ ($Y' = Y$) indicate respectively, the position of the target and projectile, in rapidity. b denotes the impact parameter. We parameterize $g^{(i)}(b)$ as

$$g^{(i)}(b) = g^{(i)} S(b) = \frac{g^{(i)}}{4\pi} m_i^3 b K_1(m_i b), \quad (3.29)$$

where, $S(b)$ is the Fourier transform of the dipole formula for the form factor $1/((1 + q^2/m_i^2)^2)$. $K_1(z)$ is the modified Bessel function of a second kind, the McDonald function, (see Ref.⁴⁷ formulae 8.4).

3.2.3. S_E for hadron-nucleus scattering

Using Eq. (3.28), and neglecting the correlations between nucleons in a nucleus, the S_E term can be written in the form:

$$S_E = - \int dY' d^2b \sum_{i=1}^2 \left\{ \Phi(Y') g^{(i)}(b) \delta(Y - Y') + \Phi(Y') \int d^2b' g^{(i)}(\vec{b} - \vec{b}') S_A(b') \delta(Y' - 0) \right\}. \quad (3.30)$$

The last term is well known, and we refer the reader to Refs^{40, 41} which, as far as we know, are the most recent papers where this derivation is based on Feynman diagrams. For heavy nuclei $|\vec{b} - \vec{b}'| \ll R_A$ and the second term in Eq. (3.30) can be replaced by:

$$\Phi(Y') \int d^2b' g^{(i)}(\vec{b} - \vec{b}') S_A(b') \xrightarrow{|\vec{b} - \vec{b}'| \ll R_A} \Phi(Y') g^{(i)} S_A(b). \quad (3.31)$$

However, in the case of not very heavy nuclei (air for example), the radii are not very large and we cannot neglect the b' dependence. $S_A(b) = \int dz \rho(z, b)$, with $\int d^2 S_A(b) = A$. ρ denotes the density of the nucleons in a nucleus.

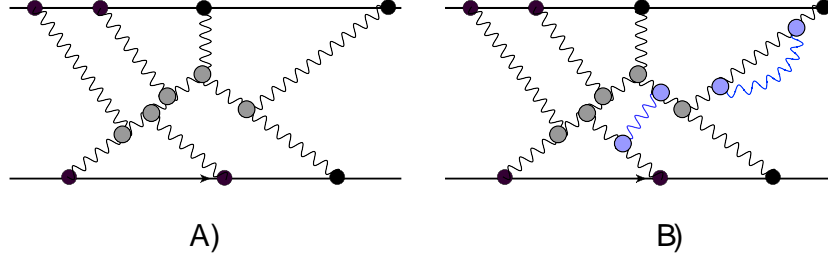


Fig. 6. The set of diagrams that contribute to the scattering amplitude of proton-proton scattering in the kinematic region given by Eq. (3.32). Fig. 6-A shows the net diagrams which are proportional to H^n . Fig. 6-B shows two examples of the diagrams which are proportional to an additional power of the small parameter Q . This figure which is proportional to an extra Q^2 was neglected. The wavy lines denote the soft Pomerons. The black circles denote $g^{(i)}$, while the gray circles describe the triple Pomeron vertices.

3.2.4. Small parameters and selection of the Pomeron diagrams

Using Eq. (3.24), Eq. (3.25), Eq. (3.26) and Eq. (3.28) we can find expressions for all experimental observables measured in proton-proton interactions*. We simplify the problem using the fact that in N=4 SYM, the vertices of the Pomeron interaction with hadrons turn out to be larger than the triple Pomeron vertex. Taking this into account we can define a new small parameter,

$$Q = \gamma^2 s^{\Delta_P} \ll 1; \quad \text{while} \quad H = g^{(i)} G_{3P} s^{\Delta_P} \geq 1 \quad (3.32)$$

The set of parameters that we will discuss below confirm our expectations. In Eq. (3.32) $\gamma^2 = \int G_{3P}^2(k_{T,1}=0, k_T, k_T) d^2 k_T$, where $k_{T,i}$ are transverse momenta of the three Pomerons. The main contributions, which are proportional to H^n stem from the 'net' diagrams of Fig. 6-a. The small parameter Q is obtained from the diagram of Fig. 6-b in which the interaction is between two Pomerons that are not attached to a proton or to the Pomeron loop diagrams (see two examples in Fig. 6-b).

3.3. Summing large Pomeron loops (Mueller-Patel-Salam-Iancu (MPSI) approximation)

As has been mentioned, the approach given by the functional integral of Eq. (3.24) can be solved.^{44,45} However, in our model we prefer to develop the approximate method of calculation which leads to a simpler set of formulae. These formulae allow us to organize the fitting procedure in an economical way. The main idea of this approximation, which we call the Mueller-Patel-Salam-Iancu (MPSI) approxi-

*We need to introduce additional phenomenological parameters to describe the main characteristics of the inelastic processes, which take into account the hadronization stage, in terms of a microscopic approach based on QCD.

mation, is the following: At high energy, in the kinematic region

$$Y \leq \frac{\Delta_P^2}{g_{3P}^2} \equiv \frac{1}{\gamma}, \quad (3.33)$$

only large Pomeron loops, with a rapidity size of the order of Y , contribute to the high energy asymptotic behaviour of the scattering amplitudes.

3.3.1. The simplest loop diagram.

The MPSI approximation has been discussed in detail in Refs.^{48–51} Here we illustrate the method using the example of the first Pomeron loop diagram given in Fig. 7. Using Eq. (3.24) or the generating function approach, we obtain the contribution of this diagram in the form

$$\begin{aligned} A(\text{Fig. 7}) &= \quad (3.34) \\ &= -g_1 g_2 G_{3P}^2 \int_0^Y dY_1 \int_0^{Y_1} dY_2 P(Y - Y_1) P^2(Y_1 - Y_2) P(Y_2 - 0) \\ &= -g_1 g_2 G_{3P}^2 \int_0^Y dY_1 \int_0^{Y_1} dY_2 e^{\Delta(Y + Y_1 - Y_2)} \\ &= -\frac{g_1 g_2 G_{3P}^2}{\Delta_P^2} \{e^{2\Delta_P Y} + e^{\Delta_P Y} + \Delta_P Y e^{\Delta_P Y}\} \\ &= -\tilde{g}_1 \tilde{g}_2 \{a_{dd}^2 e^{2\Delta_P Y} + a_{dd}^2 e^{\Delta_P Y} + \Delta_P a_{dd}^2 Y e^{\Delta_P Y}\}. \quad (3.35) \end{aligned}$$

$G_{3P} = \Delta_P a_{dd}^2$, $\tilde{g}_i = g_i / \sqrt{a_{dd}}$ (see the notation in Fig. 7).

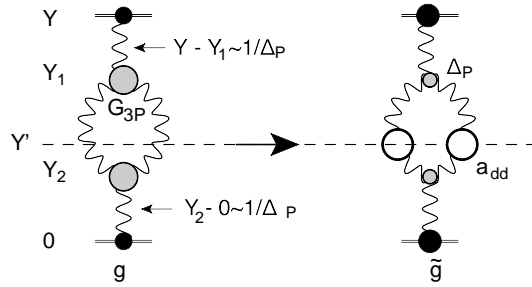


Fig. 7. MPSI approximation: an example of the first loop diagram. Wavy lines denote the BFKL Pomerons, the blob stands for the scattering amplitude (a_{dd}) of two partons and G_{3P} denotes the triple BFKL Pomerons vertex. Δ_P the Pomeron intercept while $g(\tilde{g})$ denotes the Pomeron-hadron vertex.

The main idea of the MPSI approximation is to take into account only the first term in Eq. (3.35), while neglecting other terms, since they are suppressed by $\exp[-\Delta_P Y]$. This term results from the integration of $Y - Y_1 \approx 1/\Delta_P$ and $Y_2 - 0 \approx 1/\Delta_P$ (see Fig. 7).

3.3.2. Dressed Pomeron.

In the following we utilize the MPSI approximation so as to find the sum of enhanced diagrams (see Fig. 8) which change the Green function of the Pomeron. From Fig. 8 it is clear that the MPSI approximation reduces the sum of the Pomeron loops to the product of two cascade of Pomerons, where only the splitting of one Pomeron into two, is taken into account. The Pomeron cascade satisfies Eq. (2.21), which can be reduced to the equation of the generating function:^{52–54}

$$Z(y, u) = \sum_n P_n(y) u^n, \quad (3.36)$$

where, $P_n(y)$ is the probability to find n -Pomerons at rapidity y . At rapidity $y = Y$, there is only one fastest parton (dipole), which is $P_1(y = Y) = 1$, while $P_{n>1}(y = Y) = 0$. This is the initial condition for the generating function:

$$Z(y = Y) = u; \quad Z(y, u = 1) = 1. \quad (3.37)$$

The condition at $u = 1$, follows from the physical meaning of P_n as a probability.

The generating functions of the projectile $Z^p(Y - Y')$ and the target $Z^t(Y')$ (see Fig. 8) satisfy a very simple equation that describes the parton cascades, in which a parton can only decay into two partons. This equation follows from Eq. (2.21). It has the form:

$$-\frac{\partial Z(y, u)}{\partial y} = -\Delta_P u(1 - u) \frac{\partial Z(y, u)}{\partial u}. \quad (3.38)$$

The solution of the equation above is:

$$Z(y, u) = \frac{u}{u + (1 - u)e^{\Delta_P y}}. \quad (3.39)$$

Eq. (3.39) satisfies the initial and boundary conditions of Eq. (3.37). The amplitude in the MPSI approximation has the following form:^{48, 54}

$$\begin{aligned} N^{MPSI}(Y) &= \\ &= \sum_{n=1}^{\infty} \frac{(-a_{dd})^n}{n!} \left(\frac{\partial}{\partial u^{(1)}} \right)^n Z(Y - Y'; u^{(1)} = 1) \left(\frac{\partial}{\partial u^{(2)}} \right)^n Z(Y' - 0; u^{(2)} = 1) \\ &= 1 - \exp \left\{ -a_{dd} \frac{\partial}{\partial u^{(1)}} \frac{\partial}{\partial u^{(2)}} \right\} Z(Y - Y'; u^{(1)}) Z(Y' - 0; u^{(2)}) \Big|_{u^{(1)}=u^{(2)}=1}. \end{aligned} \quad (3.40)$$

From Eq. (3.40) we can see that the MPSI approximation is the t -channel unitarity constraint adjusted to Reggeon Calculus, in the form of a generating function. From this picture we can find the sum of enhanced diagrams from the knowledge of the cascade described by the ‘fan’ diagrams. The physical meaning of the parameters are: a_{dd} is the low energy amplitude for two partons (dipoles) scattering at an arbitrary rapidity Y' , and Δ_P is the value of the vertex for the decay of one parton (dipole) to two parton (dipoles). It should be stressed that the answer does not depend on the value of Y' , which should be chosen somewhere in the central region of the scattering.

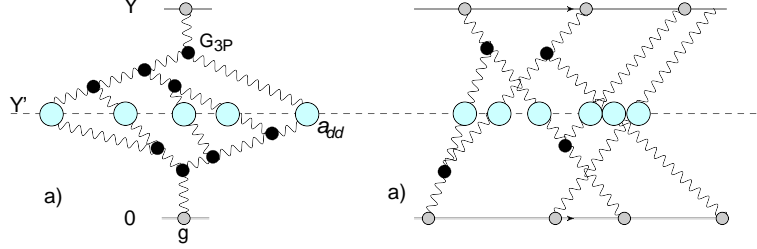


Fig. 8. MPSI approximation: enhanced diagrams (Fig. 8-a) and the net diagrams of Fig. 6-a (Fig. 8-b). Wavy lines denote the BFKL Pomeron, the blob stands for the scattering amplitude of two partons G_{3P} is the triple BFKL Pomeron vertex.

Using Eq. (3.40) we obtain the Green's function of the dressed Pomeron in a closed form:⁵¹

$$G(Y) = 1 - \exp\left(\frac{1}{T(Y)}\right) \frac{1}{T(Y)} \Gamma\left(0, \frac{1}{T(Y)}\right) \quad \text{with } T(Y) = a_{dd} e^{\Delta Y}. \quad (3.41)$$

3.3.3. Net diagrams of Fig. 6-a (Ref.⁵⁵)

Before starting the discussion on the summation of different processes in the MPSI approximation, we wish to make a general remark on our further presentation. Thus far, we have discussed the derivation of our results and the results of our computations, however, lack of space does not allow us to continue in this user friendly style. Most of the theoretical calculations are new and are dispersed over all our papers. For the convenience of the reader we have included in the titles of the subsections, the references to the relevant papers.

Using the MPSI approach, the sum of the Pomeron diagrams, with S_E given in Eq. (3.28), has been calculated in Ref.⁵⁵ An especially simple form presents the sum of the net diagrams of Fig. 6-a.⁵⁵ For the amplitude that has been introduced in Eq. (2.4), Eq. (2.5) and Eq. (2.7), we obtain:

$$A_{i,k}(Y; b) = 1 - \exp\left\{-\int d^2b' \frac{\left(\tilde{g}_i(\vec{b}')\right) \tilde{g}_k(\vec{b} - \vec{b}') T(Y)}{1 + T(Y) [\tilde{g}_i(\vec{b}') + \tilde{g}_k(\vec{b} - \vec{b}')]}\right\}. \quad (3.42)$$

3.3.4. Diffractive production (Refs.^{49, 51, 55})

As we have mentioned, the parton cascade generates the processes of diffractive production (see Fig. 4). In Fig. 4 we see that the cross section of single diffractive production is closely related to the triple Pomeron interaction. The upper Pomeron in Fig. 4 describes the process of multi-particle production by the Pomeron. The cross section of such processes is determined by $2\text{Im}P(s, t)$ which used to be called the cut Pomeron. In Ref.⁴⁹ the technique developed, allows us to calculate the cross sections of single and double diffraction in the MPSI approximation summing

Pomerons and cut Pomerons. The diagrams for these two processes are shown in Fig. 9. We sum these diagram⁵¹ and the sum has the following form

$$N_{sd}^{MPSI}(Y, Y_m = Y - Y_0 = \quad (3.43)$$

$$= \frac{\Delta_P a_{dd}^2}{6} \frac{e^{\Delta_P(2Y - Y_m)}}{T_{SD}^2(Y, Y_m)} T_{SD}((T_{SD} - 1)^2 - 2) + e^{1/T_{SD}}(1 + 3T_{SD}) \Gamma_0(1/T_{SD}),$$

$$T_{SD}(Y, Y_m) = a_{dd} \exp(\Delta_P(Y - Y_m)) \{\exp(\Delta_P Y_m) - 1\}. \quad (3.44)$$

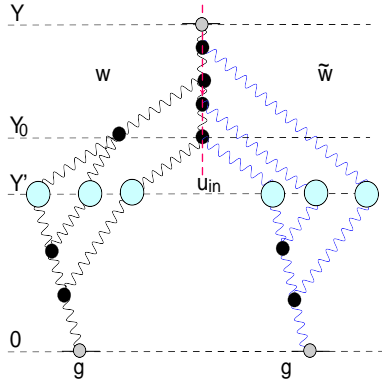


Fig. 9-a

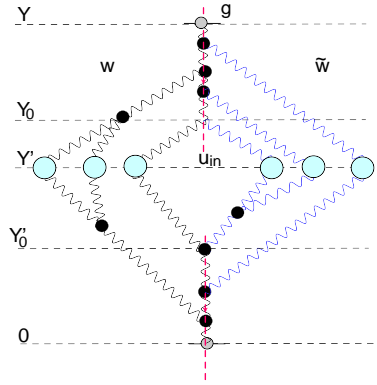


Fig. 9-b

Fig. 9. MPSI approximation: single (Fig. 9-a) and double (Fig. 9-b) diffractive production. Wavy lines denote the BFKL Pomerons, the blob stands for the scattering amplitude of two partons. G_{3P} is the triple BFKL Pomerons vertex. Wavy lines that are crossed by the dashed lines denote the cut Pomeron.

The expression for the integrated cross section for double diffraction (see Fig. 9-b) can be obtained directly from the unitarity constraint of Eq. (2.6), as the diagrams that describe the elastic and single diffraction cross sections, do not contribute to the set of Pomeron diagrams, that describe the exact Pomeron Green's function (see Fig. 8-a and Fig. 8-b). The unitarity constraint is given by:

$$2N^{MPSI} = N_{DD}^{MPSI} + N_{in}^{MPSI}, \quad (3.45)$$

where, N_{in}^{MPSI} stands for the inelastic cross section.

It was shown that N_{in}^{MPSI} is equal to $N^{MPSI}(2T(Y))$ (see Refs.^{49,56,57}). Consequently, the integrated double diffraction cross section can be written in the form:

$$N_{DD}^{MPSI}(Y) = 2N^{MPSI}(T(Y)) - N^{MPSI}(2T(Y)). \quad (3.46)$$

3.4. Qualitative features of our model.

Current IP models have changed our perception of the Regge Pomeron. Before detailing with specific features of our model, we make a few general remarks resulting from basic principles.

- Scattering amplitudes are constrained by the s-channel unitarity bound, where in the black disc limit $\sigma_{el} = \sigma_{inel} = 0.5 \sigma_{tot}$.
- The Pumplin bound⁵⁹ is a direct consequence of Eq. (2.15) and Eq. (2.16) and the unitarity constraints for the S-matrix,i.e

$$S S^+ = 1; \quad S = 1 + i \mathbf{T}; \quad i(\mathbf{T}^+ - \mathbf{T}) = \mathbf{T}^+ \mathbf{T}, \quad (3.47)$$

and can be written as:

$$\sigma_{el} + \sigma_{diff}^{GW} \leq \frac{1}{2} \sigma_{tot}. \quad (3.48)$$

σ_{diff}^{GW} is the sum of GW soft diffractive cross sections.

- Below the black disc limit, $\sigma_{el} \leq \frac{1}{2} \sigma_{tot} - \sigma_{diff}^{GW}$ and $\sigma_{inel} \geq \frac{1}{2} \sigma_{tot} + \sigma_{diff}^{GW}$.

More specific comments regarding our model:

- Our model is based on a fitted bare non screened Pomeron in a 2 channel Good-Walker (GW) system, composed of soft elastic and GW diffractive scatterings channels. Our \mathbb{P} basic parameters are $\Delta_{\mathbb{P}} = 0.2 - 0.3$ and a very small $\alpha'_{\mathbb{P}} (\approx 0.028)$.
- Since $\Delta_{\mathbb{P}}$ is non zero there is no dynamic distinction between low and high mass diffraction. We have treated the Pomeron interactions separately, as their dependence on the Pomeron parameters is different from that of the GW components.
- Our approach, based on Reggeon calculus, (see Eq. (3.24),Eq. (3.25), Eq. (3.26) and Eq. (3.28)) satisfies t-channel unitarity constraints. In practice t-channel unitarity, induced by multi \mathbb{P} interactions, leads to "high mass" GW diffraction and, consequently, additional screening of the GW sector.
- In spite of large screening, neither experimentally, nor in any of the models on the market, is the diffraction cross section small, and it does not appear to decrease even at energies of $W = 100$ TeV.
- In our two channel model two partial amplitudes ($A_{12}(s, b)$ and $A_{22}(s, b)$) reach unity at small b , but one amplitude ($A_{11}(s, b)$) is less than 1 at small b , even at $W = 100$ TeV.

As we have discussed, the LHC data led to small value of the slope of the Pomeron trajectory, which is in accord with the theoretical expectation that has been discussed above. However, at first sight, this statement is in contradiction with the measured shrinkage of the diffraction cone as a function of energy, which is considerable. Actually, this is not true if the value of the Pomeron intercept is large. To see this, it is enough to discuss the simple eikonal formula of Eq. (2.7) with Ω given by Eq. (2.17),i.e.

$$A(s, b) = i \left(1 - e^{-A_{\mathbb{P}}(s, b)} \right) = i \left(1 - \exp \left(-S(b) \left(\frac{s}{s_0} \right)^{\Delta_{\mathbb{P}}} \right) \right), \quad (3.49)$$

20 *E. Gotsman, E. Levin and U. Maor*

where (see Eq. (1.2)),

$$S(b) = \int \frac{d^2}{4\pi^2} e^{\vec{q}\vec{b}} g_p(m_1, M_1, t - q^2) g_t(m_2, M_2, t - q^2). \quad (3.50)$$

At large s , $A_P(s, b=0) \gg 1$ and $A(s, b=0) = 1$. However, at large b $S(b) \xrightarrow{mb \gg 1} \exp(-mb)$ and $A(s, b) = A_P(s, b) \ll 1$. Therefore, the typical value of b , which contributes to the integral

$$\langle b^2 \rangle = \int b^2 d^2 b A(s, b) / \int d^2 b A(s, b), \quad (3.51)$$

stems from

$$A_P(s, b=b^*) = g^2 \left(\frac{s}{s_0} \right)^{\Delta_P} \exp(-mb) \approx 1. \quad (3.52)$$

It gives

$$b^* = \frac{\Delta_P}{m} \ln(s/s_0) + R_0 \approx 1/m. \quad (3.53)$$

Therefore, $\langle b^2 \rangle = \left(\frac{\Delta_P}{m} \ln(s/s_0) + R_0 \right)^2$. One can see that if $\Delta_P = 0.2 \div 0.3$ and $m \sim 1 \text{ GeV}$ \dagger $\langle b^2 \rangle = R_0^2 + 2 \frac{\Delta_P}{m} \ln(s/s_0) + \left(\frac{\Delta_P}{m} \ln(s/s_0) \right)^2 \rightarrow R_0^2 + 2 \frac{\Delta_P}{m} \ln(s/s_0) = R_0^2 + 2(0.2 \div 0.3) \ln(s/s_0)$. This value of the average b^2 is close to the experimental one.

4. Physical observables in our model.

4.1. Classical soft Physics (Refs.^{51,55})

4.1.1. Total and elastic cross sections

We start with the formulae for the classical set of soft interaction data at high energy: total, elastic and diffractive dissociation cross sections. In our two channel approximation for the Good-Walker mechanism, the elastic amplitude has the following form:

$$a_{el}(s, b) = i \left(\alpha^4 A_{1,1} + 2\alpha^2 \beta^2 A_{1,2} + \beta^4 A_{2,2} \right). \quad (4.54)$$

- Note the elastic amplitude $a_{el}(s, b) = 1$, when, and only when, $A_{1,1}(s, b) = A_{1,2}(s, b) = A_{2,2}(s, b) = 1$.
- When $a_{el}(s, b) = 1$, all diffractive amplitudes at the same values of (s, b) vanish (see Eq. (4.59)).

[†]As has been mentioned in section 2.1.2 m was expected to be approximately the pion mass. However, in Ref.⁶¹ arguments have been provided that m could be a mass of the lightest glueball. $m \sim 1 \text{ GeV}$ is a reasonable estimate.

$A_{i,k}$ are given by

$$\begin{aligned} A_{i,k}(Y; b) &= 1 - \exp\left(-\frac{1}{2}\Omega_{ik}^P(s, b)\right) \\ &= 1 - \exp\left\{-\int d^2b' \frac{\left(\tilde{g}_i(\vec{b}') \tilde{g}_k(\vec{b} - \vec{b}') G(Y)\right)}{1 + G(Y) [\tilde{g}_i(\vec{b}') + \tilde{g}_k(\vec{b} - \vec{b}')]}\right\}. \end{aligned} \quad (4.55)$$

$G(Y)$ is given by Eq. (3.41). Eq. (4.55) can be obtained from Eq. (3.41) by the replacement $T(Y) \rightarrow G(Y)$. It reflects the fact that in Eq. (4.55) we have replaced the ‘bare’ Pomeron by the dressed one. The physical observables can be calculated using the following set of formulae which stem from the unitarity constraint of Eq. (2.6):

$$\sigma_{tot}(s) = 2 \int d^2b \operatorname{Im} a_{el}(s, b); \quad \sigma_{el}(s) = \int d^2b |a_{el}(s, b)|^2; \quad (4.56)$$

$$d\sigma_{el}/dt = \pi |f(s, t)|^2; \quad \sigma_{tot} = 4\pi \operatorname{Im} f(s, t); \quad a_{el}(s, b) = \frac{1}{2\pi} \int d^2q e^{i\vec{q} \cdot \vec{b}} f(s, t = -q^2);$$

$$\sigma_{in}(s) = \int d^2b G^{in}(s, b) \quad \text{with} \quad G^{in}(s, b) = \alpha^4 G_{1,1}^{in} + 2\alpha^2 \beta^2 G_{1,2}^{in} + \beta^4 G_{2,2}^{in} \quad (4.57)$$

$$B_{el} = \int d^2b b^2 \operatorname{Im} a_{el}(s, b) / \left(2 \int d^2b \operatorname{Im} a_{el}(s, b)\right). \quad (4.58)$$

4.1.2. Diffractive production cross sections

In our model we have two sources leading to diffractive production:⁵⁵ the first one is due to Good-Walker mechanism in two channel model, and the second stems from the enhanced diagrams of Fig. 9-a. As we have mentioned, when $\Delta_P \neq 0$, there is no difference between the origins of the two, and we shall call the second one ‘large mass diffraction’. The Good-Walker term has the following form:

$$\sigma_{SD}^{GW} = \int d^2(\alpha\beta\{-\alpha^2 A_{1,1} + (\alpha^2 - \beta^2)A_{1,2} + \beta^2 A_{2,2}\})^2. \quad (4.59)$$

$A_{i,k}$ are given by Eq. (4.55) and the term which describes diffractive production in the region of large mass,

$$\sigma_{SD}^{\text{Large mass}} = 2 \int dY_m \int d^2b \quad (4.60)$$

$$\{\alpha^6 A_{1,1,1}^{SD} + \alpha^2 \beta^4 A_{1,2,2}^{SD} + 2\alpha^4 \beta^2 A_{1,1,2}^{SD} + \beta^2 \alpha^4 A_{2,1,1}^{SD} + 2\beta^4 \alpha^2 A_{2,1,2}^{SD} + \beta^6 A_{2,2,2}^{SD}\},$$

with,

$$\begin{aligned} A_{i;k,l}^{SD}(Y, Y_m) &= \\ &\int d^2b' 2\Delta e^{-\Delta Y_m} T_{SD}^2(Y, Y_m) \tilde{g}_i \sqrt{\tilde{g}_k \tilde{g}_l} e^{-2\tilde{g}_i - \tilde{g}_k - \tilde{g}_l} \int \frac{d\xi_2 d\bar{\xi}_2 \sqrt{\xi_2 \bar{\xi}_2}}{(1 + (\xi_2 + \bar{\xi}_2) \cdot T_{SD})^2} e^{-\xi_2 - \bar{\xi}_2} \\ &\times J_1\left(2\sqrt{\tilde{g}_k \xi_2}\right) J_1\left(2\sqrt{\tilde{g}_l \bar{\xi}_2}\right) \left\{1 - \exp\left(\frac{-\tilde{g}_i}{1 + \xi_2 T_{SD}}\right)\right\} \left\{1 - \exp\left(\frac{-\tilde{g}_i}{1 + \bar{\xi}_2 T_{SD}}\right)\right\}. \end{aligned} \quad (4.61)$$

22 *E. Gotsman, E. Levin and U. Maor*

\tilde{g}_i , in Eq. (4.61), denotes $\tilde{g}_i(\vec{b}')$. Similar notations apply to \tilde{g}_k and \tilde{g}_l .

$$T_{SD}(Y; Y_m = \ln(M^2/s_0)) = a_{dd} (e^{\Delta Y_m} - 1) e^{\Delta(Y-Y_m)}. \quad (4.62)$$

The same two mechanisms contribute to double diffractive production leading to:

$$\sigma_{DD}^{GW} \int d^2b \alpha^2 \beta^2 \{-\alpha^2 A_{1,1} + (\alpha^2 - \beta^2) A^{1,2} + \beta^2 A_{2,2}\}^2. \quad (4.63)$$

$A_{I,k}$ are given by Eq. (4.55) and the term which is determined by the Pomeron interaction (see Fig. 9-b), which contribute to the large masses:

$$\sigma_{DD}^{\text{Large mass}} = \int d^2b \{\alpha^4 A_{1,1}^{DD} + 2\alpha^2 \beta^2 A_{1,2}^{DD} \beta^4 A_{2,2}^{DD}\}. \quad (4.64)$$

$$\begin{aligned} A_{i,k}^{DD}(Y; b) &= 2A_{i,k}^{el}(T(Y); b) - |A_{i,k}^{el}(T(Y); b)|^2 \\ &- 2 \int dY_m A_{i,k,k}^{SD}(T_{SD}(Y, Y_m; b); b) - A_{i,k}^{in}(2T(Y); b). \end{aligned} \quad (4.65)$$

4.2. Estimates of the value of parameters and the range of applicability

Our model has a set of parameters, determined by fitting the experimental data. The advantage of our model is that for some of these parameters we can utilize estimates obtained from matching with pQCD.

$$\Delta_P \propto \bar{\alpha}_S; \quad G_{3P} \propto \bar{\alpha}_S^2; \quad g_i \propto 1, \quad (4.66)$$

which leads to $\gamma \ll \Delta_P \ll g_i$.

To estimate the range of energy where the MPSI approximation is valid, we notice that the most dangerous term in Eq. (3.35) is the last one, which is proportional to $\Delta_P a_{dd}^2 Y$. Such terms lead to the renormalization of the Pomeron intercept. In order to neglect them, we have to restrict the range of Y by

$$\Delta_P a_{dd}^2 Y < 1; \quad Y < \frac{1}{a_{dd}^2 \Delta_P} = \frac{1}{\gamma}. \quad (4.67)$$

In our approach we did not take into account the four Pomeron interaction. As shown in Ref.³⁴ this interaction becomes important when $Y > (2/\Delta_P) \ln(1/\alpha_S)$ and its strength is approximately $a_{dd}^2 = \gamma/\Delta_P$. We will see below that our fit requires $\Delta_P \approx 0.23$ and $\gamma = 0.0045$, which leads to small $a_{dd}^2 \approx 0.015$. Therefore, the value of Y , for which we need to include the four Pomeron interaction, is approximately $Y \sim 50 \div 60$.

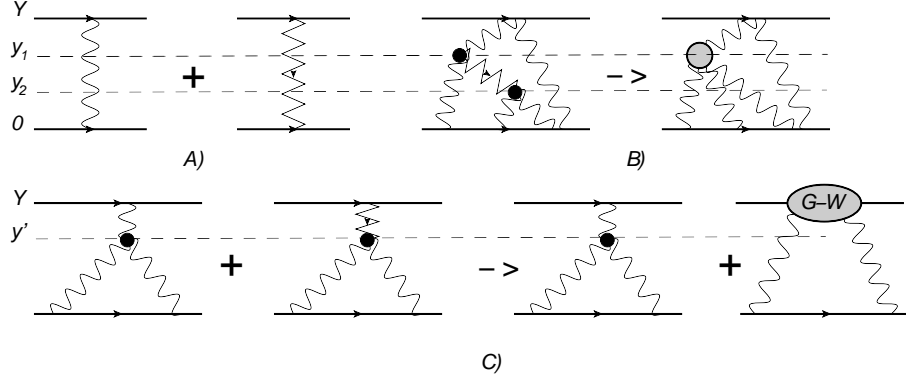


Fig. 10. Contributions of secondary Reggeons denoted by zigzag lines. Wavy lines denote the Pomeron. Fig. 10-A shows the contribution to the scattering amplitude due to exchange of Pomeron and Reggeon. Fig. 10-B and Fig. 10-C illustrate that the exchange of secondary Reggeons can be reduced to inclusion of the vertices for the Pomeron-Pomeron interaction, or can be included into Good-Walker mechanism.

4.3. Data and fitting procedure

4.3.1. Data prior to the LHC era

We started constructing our model in 2007, prior to the commissioning of the LHC. At that time the highest energy accelerator data available was that emanating from the Tevatron at $W = 1.8$ TeV. There were two incompatible measurements available for the total cross section at that energy. That of the CDF collaboration³⁵ which gave a value of 80.03 ± 2.24 mb, and the second by the E710 collaboration³⁶ which published a value of 72.1 ± 3.3 mb. The E710 value was close to that predicted by the Donnachie-Landshoff formalism,⁵ and in accord with the values cited by most models (including GLM).

Currently, with the publication of the LHC total cross section by the TOTEM collaboration,⁴ i.e. $\sigma_{tot} = 98.6 \pm 2.2$ mb at $W = 7$ TeV, most models that reproduce this value, are in accord with the CDF measurement at $W = 1.8$ TeV. There is a lesson to be learnt from this, that experimental results should not be discriminated against, on the basis of theoretical prejudice!

4.3.2. Low energy behaviour of the scattering amplitude

As we shall see in the next section, most of our data base consists of lower energy points from ISR and Sp \bar{p} S/SppS ($W \approx 20$ -70 GeV), where the contribution of the secondary Regge exchanges are important. A secondary Reggeon has an energy behaviour $\exp(\Delta_R(Y - 0))$. The sum $\mathbb{P} + \mathbb{R}$ describes the energy behaviour of the elastic scattering amplitude without screening corrections. This sum replaces the single Pomeron exchange in the definition of Ω_{ik} . Inserting this sum everywhere in the more complicated diagram (see Fig. 10), one can see that the integrations over rapidities reduces the contributions of the secondary Reggeons. By introducing new

vertices for the Pomeron-Pomeron interactions (see Fig. 10-B) the integration over $y_1 - y_2$ can be replaced by a new $\mathbb{P} \rightarrow 3\mathbb{P}$ vertex, or it can be absorbed into G-W mechanism (see Fig. 10-C). Since in our approach the vertices, other than the triple Pomeron vertex are considered to be small, we arrive at the conclusion that for lower energies we only need to replace the single Pomeron exchange by $\mathbb{P} + \mathbb{R}$, in the definition of Ω_{ik} .

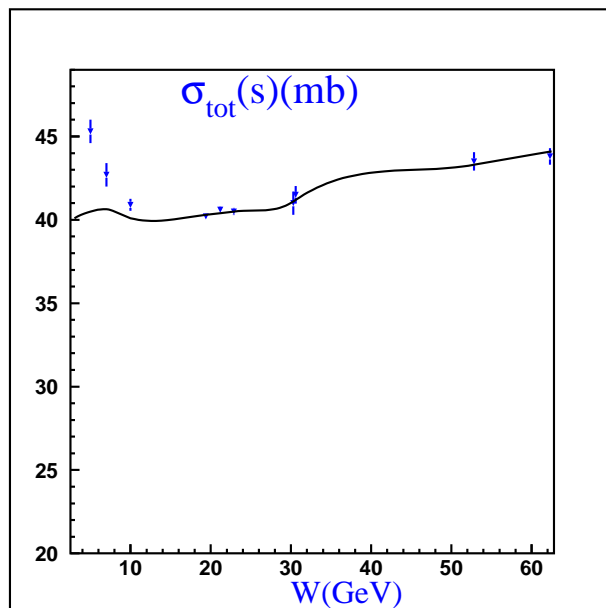


Fig. 11. Behavior of the total cross section $\frac{1}{2}[\sigma_{\bar{p}p} + \sigma_{pp}]$ at low energies

In Fig. 11 we compare our prediction for lower energies with the experimental data and obtain a satisfactory description to within 10%. The conclusion is very simple: we do not need an additional source to describe the lower energy behaviour of the amplitude.

4.3.3. The fit to the data and its phenomenology

4.3.3.1. The main formulae of the fit The main formulae, that we have derived from Eq. (3.26), Eq. (3.27), Eq. (3.28) and Eq. (3.29), are written in Eq. (4.54). Note that g_i in Eq. (4.54) have dimension of inverse momentum (see Eq. (2.23)) as well as $G_{3\mathbb{P}}$, while γ is dimensionless. Actually $\gamma^2 = \int d^2k G_{3\mathbb{P}}^2$, but because we do not know the dependence of $G_{3\mathbb{P}}$ with respect to the transverse momenta of Pomerons, we consider γ and $G_{3\mathbb{P}}$ as independent parameters of the fit.

We deal with the secondary reggeon in the same way as in Ref.⁵¹ adding Ω^R to

Ω^P in Eq. (4.54), i.e.

$$\Omega_{ik}(s, b) = \Omega_{ik}^P(s, b) + \Omega_{ik}^R(s, b). \quad (4.68)$$

Ω^R is taken in the following form:

$$\Omega_{ik}^R(s, t) = g_i^R g_k^R \eta(t) e^{-\left(\frac{1}{4}(R_{0i}^2 + R_{0k}^2) + \alpha'_{\mathcal{R}} \ln(s/s_0)\right) |t|} \left(\frac{s}{s_0}\right)^{\Delta_{\mathcal{R}}}, \quad (4.69)$$

with the signature factor $\eta(t)$ which is equal to

$$\eta(t) = \frac{1 \pm e^{i\pi\alpha_{\mathcal{R}}(t)}}{\sin(\pi\alpha_{\mathcal{R}}(t))}. \quad (4.70)$$

4.3.3.2. The strategy of our fitting procedure. In our model the Pomeron is specified by nine parameters, the Tevatron data (which was the highest energy data available at that time) on its own is not sufficient to determine the parameters. Consequently, we have also to include ISR - Sp \bar{p} S/Sp p S lower energy ($W \approx 20$ -70 GeV) data. This data has small errors which facilitate a reasonably reliable fit. To reduce the number of Reggeon parameters, we define $\sigma_{tot} = \frac{1}{2}(\sigma_{tot}(pp) + \sigma_{tot}(p\bar{p}))$. The inclusion of the Regge sector of our fit requires five additional parameters. i.e. we have fourteen parameters in all.

Our data base has 58 experimental data points, which include the average i.e. ($\sigma_{tot} = \frac{1}{2}(\sigma_{tot}(pp) + \sigma_{tot}(p\bar{p}))$), integrated elastic cross sections, integrated single and double diffraction cross sections, B_{el} , to which we have added a consistency check of the CDF data $\frac{d\sigma_{el}}{dt}$ ($-t \leq 0.5 \text{ GeV}^2$), $\frac{d^2\sigma_{sd}}{dt dM^2/s}$ ($-t = 0.05 \text{ GeV}^2$) and B_{sd} . The data points were fitted to determine the 14 free parameters of our model. We fit the entire data base simultaneously.

4.3.3.3. The results of the fit (prior the LHC) Our fit is based on 58 experimental data points. The model gives a good reproduction of the data, with a $\chi^2/d.o.f. = 1.56$. However, a large contribution to the value of $\chi^2/d.o.f.$ stems from the uncertainty of the value of two single diffraction cross sections, and of the CDF total cross section³⁵ at the Tevatron ($W = 1.8 \text{ TeV}$). Neglecting the contribution of these three points to the total χ^2 we obtain $\chi^2/d.o.f. = 0.86$.

4.3.4. Comments on the parameter values of the fit

It should be stressed that the value of our phenomenological parameters (see Table 1) are in agreement with the theoretical estimates of Eq. (4.66). We obtain a value of $\alpha'_{\mathcal{P}} = 0.028$, which is sufficiently close to zero to justify our approximation of taking $\alpha'_{\mathcal{P}} = 0$ in our summation of diagrams. Choosing the typical soft scale $\mu = 1 \text{ GeV}$ we can see that $g_i\mu \approx 1$ and

$$G_{3P}\mu \approx \gamma \approx \Delta_{\mathcal{P}}^2 \ll \Delta_{\mathcal{P}} \ll g_i\mu. \quad (4.71)$$

As we have discussed, we sum all diagrams in an approximation in which $g_i G(T(Y)) \geq 1$ while $\Delta_{\mathbb{P}}^2 G(T(Y)) \ll 1$. The values of the fitted parameters support the use of this approximation.

As mentioned previously, most models for soft interactions, which were proposed prior to the measurements at the LHC, are only marginally compatible with LHC data, our GLM model has the same deficiency. We investigated possible causes of the problem, by considering separate fits to the high energy ($W > 500 \text{ GeV}$), and low energy ($W < 500 \text{ GeV}$) data. Our output results are moderately higher than our previous predictions. Our results for total and elastic cross sections are systematically lower than the recent Totem and Alice published values, while our results for the inelastic and forward slope agree with the data. If, with additional experimental data, the errors will be reduced, while the central cross section values remain unchanged, we will need to reconsider the physics on which our model is built. Our procedure for adjusting parameters may be deficient, requiring a more sophisticated data analysis which may yield satisfactory results. Recall that the fitted data base⁶ contained no LHC data. Moreover, the low energy ($W < 500 \text{ GeV}$) total, elastic and diffractive cross sections which constitute the major portion of the fitted data points have rather small errors. Consequently, our fitting procedure is not well balanced as the main contribution to our $\chi^2/d.o.f.$ stems from the low energy data.

To check the second option, we removed the low energy data and fitted only the high energy data ($W > 500 \text{ GeV}$), including the available LHC soft cross section data points, so as to determine the Pomeron parameters. Having adjusted these parameters, we tuned the value of the Reggeon-proton vertex, which enabled us to obtain a smooth cross section behaviour through the ISR-LHC energy range. We hoped that this exercise would clarify to what extent our model has intrinsic deficiencies, or do we just have a technical problem in the procedure for adjusting our free parameters.

At this stage we were fairly pessimistic about our model reproducing all the "soft physics" data emanating from LHC and concluded our paper⁵¹ as follows: "In spite of the fact that the values of the parameters, extracted from our current fitting, are slightly different from our previous values, the overall picture remains unchanged. Our updated total and elastic cross sections are slightly lower than the published TOTEM values,⁴ but still within the relatively large experimental error bars. Should future LHC measurements confirm the present TOTEM values, we will need to revise our dynamic picture for soft scattering."

4.3.5. *Success at last*

In our last paper⁸⁰ we found a set of parameters in our model for soft interactions at high energy, that successfully describes all high energy experimental data, including the LHC data. This model is based on a single Pomeron with a large intercept $\Delta_{\mathbb{P}} = 0.23$, and a slope $\alpha'_{\mathbb{P}} = 0.028(\approx 0)$, that describes both long and short

distance processes. It also provides a natural matching with perturbative QCD. All features of our model are similar to the expectations of N=4 SYM, which at present is the only theory that is able to treat strong interactions on a theoretical basis.

In this paper we retract the pessimistic concluding statement we had in⁸⁰ as we find that the conclusion was premature. The set of parameters in our previous paper was found by fitting all data with energy $W \geq 500\text{GeV}$, including the LHC data. In the present version of our GLM model⁸⁰ we made no changes other than tuning the 3 Pomeron parameters. Our tuned Δ_P changes from 0.21 to 0.23, while G_{3P} and γ the Pomeron-proton vertex, are unchanged. The small change in the value of Δ_P is sufficient to produce the desired results in our σ_{tot} and σ_{el} output values for LHC energies, while the changes in the output values of the other observables are small enough not to spoil the good reproduction of the data achieved in Ref.⁷⁸ Taking $\alpha'_P = 0$, allows us to sum all diagrams having Pomeron interactions.⁶ This is the great advantage of such an approach. In our model we only take into account the triple Pomeron interaction vertices (G_{3P}), this provides a natural matching to the hard Pomeron, since at short distances $G_{3P} \propto \alpha_S^2$, while other vertices are much smaller.

4.3.6. Results

The output of our current model is presented in Fig. 12, in which we display our calculated cross sections and forward elastic slope. It is interesting to compare the quality of our present results with our previous output.⁷⁸ Recall that the two fits have almost identical values for the free parameters, with a single change of Δ_P from 0.21 to 0.23.

We list the main features of our results:

- The main feature of our present calculation is the excellent reproduction of TOTEM's values for σ_{tot} and σ_{el} . The quality of our good fit to B_{el} is maintained. As regards σ_{inel} , our results are in accord with the higher alues obtained by ALICE¹ and TOTEM;⁴ ATLAS² and CMS³
- The quality of our output at lower energies, when compared with ISR data, is not as good as our previous results,⁷ but still acceptable. Recall that Reggeon exchange, which is included in our model, plays an important role at the low energy end of our data, and a negligible role at higher energies. As our main goal is to provide a good description of the LHC data, we have not tuned the Reggeon parameters, which could lead to an improved characterization of the ISR measurements.
- An interesting observation is that our updated output strongly supports the CDF total and elastic cross sections rather than the E710 values.³⁶ This is a common feature of other models,^{5,8} that have succeeded in reproducing the TOTEM results^{4,62} by making a radical change in their modelings.
- Note that our model is the one of the few which achieves a good reproduc-

tion of ISR diffraction, and a reproduction of the diffractive cross sections at higher energies (as shown in Fig. 12-d and Fig. 12-e).

- Our reproduction of SD and DD cross sections is complicated by the lack of common definitions of signatures and mass bounds on the diffractive components. All models on the market have introduced at least two different mechanisms to describe diffraction production. In our model these two mechanisms are: the Good-Walker production of the diffraction state with finite unspecified mass (which is independent of energy and of the values of the parameters in our model); and the diffraction due to Pomeron interactions, where the typical mass depends on Δ_P . In other models (see Refs.⁷⁻⁹) the two different mechanisms are called: "low mass" diffraction and "high mass" diffraction.
- Our calculated $d\sigma_{el}(t \leq 0.55 \text{ GeV}^2)/dt$ is presented in Fig. 15 together with the corresponding data. The quality of the fit is very good in this region of t . It shows that the impact parameter dependence of the model does not change considerably and reproduces the experimental data as well, as in our previous version of the model. We refrain from trying to reproduce the diffractive dip and higher t cross sections since our model is confined to the forward cone.
- Table 3 summarizes our calculated cross sections and B_{el} at 1.8 - 57 TeV. The Table provides the predicted values of the cross sections and forward slope at 8, 14 and 57 TeV.

Considering the energy behaviour of $\sigma_{inel}/\sigma_{tot}$, the values of this ratio given by our model are $\sigma_{inel}/\sigma_{tot} = 0.77$ at Tevatron energies decreasing to 0.73 at 57 TeV.

The origin of such a slow approach to the black disc limit of 0.5, turns out to be the same as with our previous set of parameters (see Ref.⁷⁸): where one of the partial scattering amplitude, $A_{1,1}(s, b) < 1$ at all energies, while $A_{1,2}(s, b) \approx A_{2,2}(s, b) = 1$ for $b = 0$ at the same energies.

The comparison of our results with experimental data for σ_{tot} , σ_{el} , B_{el} , σ_{sd} , σ_{dd} , and σ_{inel} are shown in Fig. 12.

Table 1. Fitted parameters for our model. The quality of the fit is $\chi^2/d.o.f. = 0.86$

Δ_P	β	α'_P GeV^{-2}	g_1 GeV^{-1}	g_2 GeV^{-1}	m_1 GeV	m_2 GeV	γ	G_{3P} GeV^{-1}	\tilde{g} GeV^{-1}
0.23	0.46	0.028	1.89	61.99	5.045	1.71	0.0045	0.03	14.6

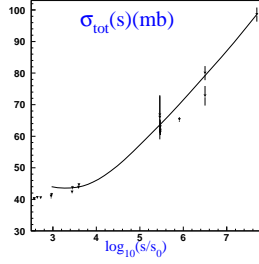


Fig. 12-a

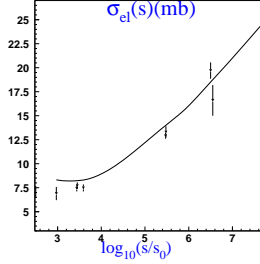


Fig. 12-b

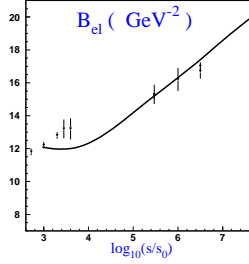


Fig. 12-c

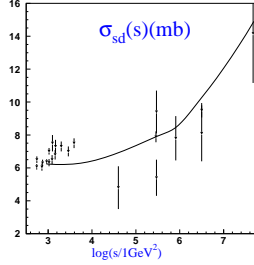


Fig. 12-d

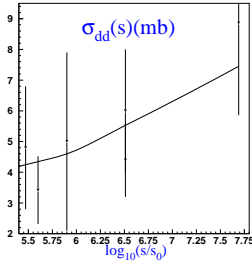


Fig. 12-e

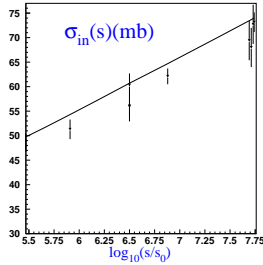


Fig. 12-f

Fig. 12. Comparison with the experimental data: the energy behaviour of the total (Fig. 12-a), elastic (Fig. 12-b), elastic slope (B_{el}) (Fig. 12-c), single diffraction (Fig. 12-d), double diffraction (Fig. 12-e), and inelastic (Fig. 12-f) cross sections. The solid lines show our present fit. The data has been taken from Ref.¹² for energies less than the LHC energy. At the LHC energy for total and elastic cross section we use TOTEM data⁴ and for single and double diffraction cross sections are taken from Ref.¹

Table 2. Fitted parameters for the secondary Reggeon in our fit.

Δ_R	α'_R GeV^{-2}	g_1^R GeV^{-1}	g_2^R GeV^{-1}	$R_{0,1}^2$ GeV^{-1}
-0.47	0.4	13.5	800	4.0

4.4. Our partial amplitudes and comparison with other models on the market

4.4.1. Amplitudes

The Good-Walker formalism²² provides an explicit form for the various elastic and diffractive amplitudes. Until recently most of the comparison of models has been confined to the level of cross-sections (which are areas), and only reveal the energy dependence, and do not display other features. Having the behaviour of the various amplitudes as functions of impact parameter (momentum transfer) would be more revealing. Unfortunately, there is a paucity of material available on amplitudes, and most refer only to the elastic amplitudes e.g.⁶³ In Fig. 13-a we show elastic

Table 3. Experimental data versus GLM model.

W	$\sigma_{tot}^{model}(mb)$	$\sigma_{tot}^{exp}(mb)$	$\sigma_{el}^{model}(mb)$	$\sigma_{el}^{exp}(mb)$
7 TeV	98.6	TOTEM: 98.6 ± 2.2	24.6	TOTEM: 25.4 ± 1.1
W	$\sigma_{in}^{model}(mb)$	$\sigma_{in}^{exp}(mb)$	$B_{el}^{model}(GeV^{-2})$	$B_{el}^{exp}(GeV^{-2})$
7 TeV	74.0	CMS: $68.0 \pm 2^{syst} \pm 2.4^{lumi} \pm 4^{extrap}$ ATLAS: $69.4 \pm 2.4^{exp} \pm 6.9^{extrap}$ ALICE: $73.2 (+2./-4.6)^{model} \pm 2.6^{lumi}$ TOTEM: $73.5 \pm 0.6^{stat} \pm 1.8^{syst}$	20.2	TOTEM: 19.9 ± 0.3
W	$\sigma_{sd}^{model}(mb)$	$\sigma_{sd}^{exp}(mb)$	$\sigma_{dd}^{model}(mb)$	$\sigma_{dd}^{exp}(mb)$
7 TeV	$10.7^{GW} + 4.18^{nGW}$	ALICE : $14.9(+3.4/-5.9)$	$6.21^{GW} + 1.24^{nGW}$	ALICE: 9.0 ± 2.6
W	$\sigma_{tot}^{model}(mb)$	$\sigma_{tot}^{exp}(mb)$	$\sigma_{in}^{model}(mb)$	$\sigma_{in}^{exp}(mb)$
57 TeV	130	AUGER: $133 \pm 13^{stat} \pm 17^{sys} \pm 16^{Gl}$	95.2	AUGER: $92 \pm 7^{stat} \pm 11^{syst} \pm 7^{Gl}$

amplitudes emanating from the GLM model for various energies. We note the overall gaussian shape of the elastic amplitudes for all energies $0.545 \leq W \leq 57$ TeV, with the width and height of the gaussian growing with increasing energy. For small values of b , the slope of the amplitudes decreases with increasing energy. The elastic amplitude (as $b \rightarrow 0$) becomes almost flat for $W = 57$ TeV, where it is still below the Unitarity limit $A_{el} = 1$.

In Fig. 13-b we show the energy behaviour of the GLM (G-W contribution) of the single diffractive amplitude as a function of impact parameter for different energies, and in Fig. 13-c we display the behaviour of the double diffractive amplitude. A common feature of both diffractive amplitudes is that with increasing energy the peaks broaden and become more peripheral. We can see in Fig. 13 – d that the partial amplitudes have different b (impact parameter) behaviour, $A_{1,2}$ approaches the black disc limit at $b \approx 1$ fm, while $A_{2,2}$ is already at the black disc limit at $b \approx 2.2$ fm, while the third amplitude $A_{1,1}$ is always less than the black disc limit. This is the reason that our elastic amplitude Fig. 13-a does not reach the black disc limit.

Kopeliovich, et al⁶⁴ have calculated the proton-proton elastic amplitude within the framework of a two scale dipole model. We show their result in Fig. 14-a, as well as that of Ferreira, Kodama and Kohara⁶⁵ who have recently made a detailed study of the proton-proton elastic amplitude for center of mass energy $W = 7$ TeV, based on the Stochastic Vacuum Model.

Fig. 14-a we compare the GLM, KPPS and FKK elastic amplitudes at $W = 7$ TeV as a function of the impact parameter. Although the shapes are similar, the KPPS and FKK amplitudes have lower intercepts at $b = 0$. If we normalize the FKK amplitude to the GLM value at $b = 0$, we note that the amplitudes which are gaussian in shape, have very similar behaviour as a function of the impact parameter. In Fig. 14-c we show the single diffraction amplitude as given by the DIPSY Monte Carlo⁶⁶ (dashed line) at $W = 1.8$ and 14 TeV. This includes contributions

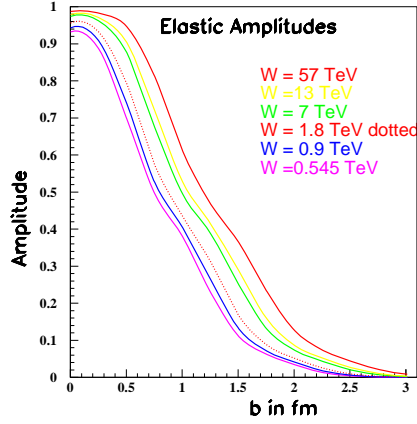


Fig. 13-a

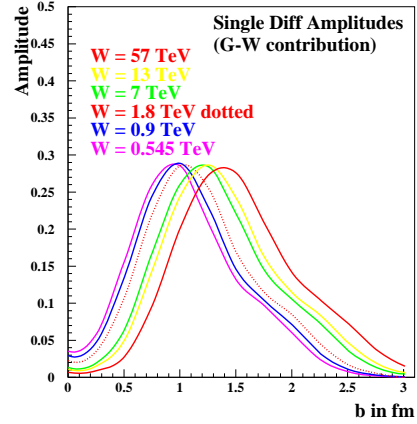


Fig. 13-b

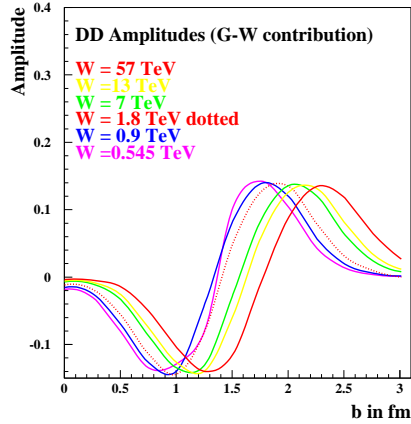


Fig. 13-c

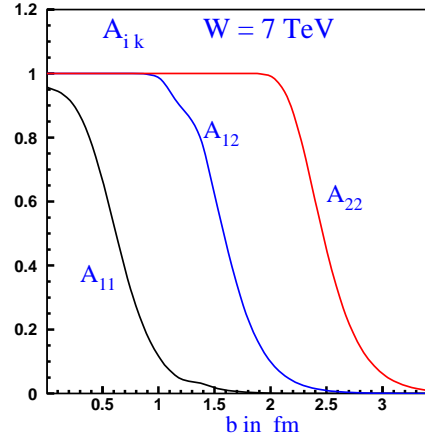


Fig. 13-d

Fig. 13. Fig. 13-a: GLM elastic amplitudes. Fig. 13-b: GLM-GW single diffraction amplitudes. Fig. 13-c: GLM double diffractive amplitudes and Fig. 13-d: the partial amplitude at the LHC energy ($W = 7$ TeV) in our model

both from the Good-Walker sector and enhanced and semi-enhanced sector. The full line is the GLM amplitude which only contains the Good-Walker contribution. Note that, although the amplitudes for the same value of W , peak at the same value of b , the DIPSY amplitudes are broader and higher, due to the additional enhanced contributions. For historical purposes we mention that the impact parameter behaviour of our diffractive amplitudes are in accord with the estimates of Miettinen and Pumplin⁶⁰ made over 35 years ago.

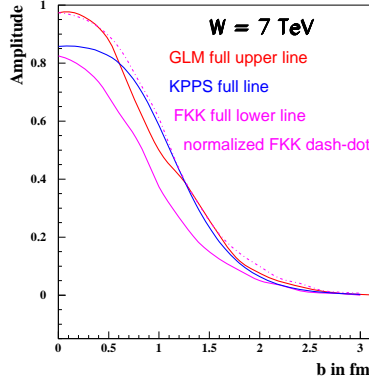


Fig. 14-a

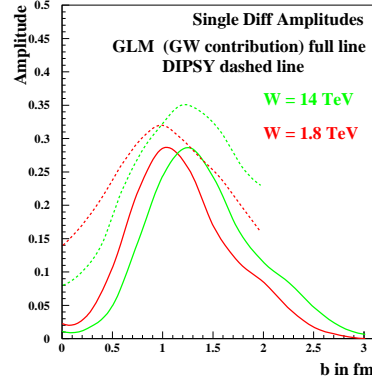


Fig. 14-b

Fig. 14. Fig. 14-a: Comparison of the elastic amplitude at 7 TeV determined by FKK,⁶⁵ KPPS⁶⁴ and GLM. Fig. 14-b: Comparison of single diffraction amplitude, dashed line DIPSY⁶⁶ (which includes enhanced and semi-enhanced contributions) and full line GLM (only GW contribution)

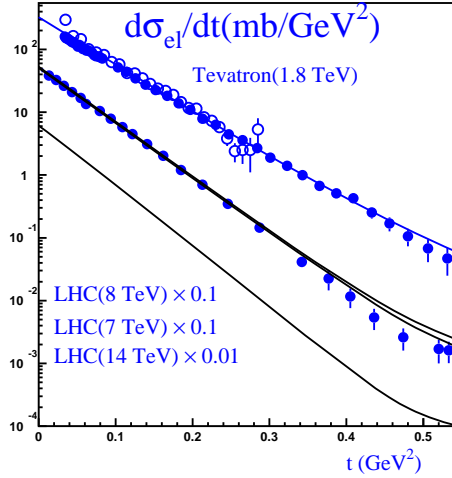


Fig. 15. $d\sigma_{el}/dt$ versus $|t|$ at Tevatron (blue curve and data)) and LHC (black curve and data) energies ($W = 1.8 TeV$, $8 TeV$ and $7 TeV$ respectively) The solid line without data shows our prediction for $W = 14 TeV$.

4.4.2. Other models on the market

Ostapchenko⁶⁸ [pre LHC] has made a comprehensive calculation in the framework of Reggeon Field Theory, based on the resummation of both crossed and semi-enhanced Pomeron diagrams. To fit the total and diffractive cross sections he assumes two Pomerons: (for his solution set C) "Soft Pomeron" $\alpha^{Soft} = 1.14 + 0.14t$

and a "Hard Pomeron" $\alpha^{Hard} = 1.31 + 0.085t$. His results are quoted in Table 4, in the column Ostap(C).

Kaidalov and Poghosyan⁶⁷ have proposed a model which is based on Regge calculus, where they attempt to describe data on soft diffraction taking into account all possible non-enhanced absorptive corrections to three Reggeon vertices and loop diagrams. It is a single Pomeron model plus secondary Regge poles, they have a Pomeron intercept $\Delta_P = 0.12$ and a Pomeron slope $\alpha'_P = 0.22 \text{ GeV}^{-2}$. The KP model forms the basis of the Monte Carlo program used by the ALICE collaboration to analyze their soft scattering data. The predictions of Kaidalov-Poghosyan⁶⁷ appear in Table 4, in the column KP.

Ciesielski and Goulianos have proposed an "event generator"⁷¹ which is based on the MBR-enhanced PYTHIA8 simulation. In Table 4 their results are denoted by MBR.

The Durham group's approach for describing soft hadron-hadron scattering⁶⁹ is similar to the GLM⁶ approach, they include both enhanced and semi-enhanced diagrams. The two groups utilize different techniques for summing the multi-Pomeron diagrams. The Durham Group⁷⁰ to be consistent with the TOTEM result,⁴ have a model, based on a three channel eikonal description, with three diffractive eigenstates of different sizes, but with only one Pomeron. $\Delta_P = 0.14$; and $\alpha'_P = 0.1 \text{ GeV}^{-2}$. Which we will refer to as KMR3C.

Recently KMR⁷² suggested a two channel eikonal model where the Pomeron couplings to the diffractive eigenstates depend on the collider energy. They have four versions of the model. The parameters of the Pomeron of their "favoured version" Model 4 are: $\Delta_P = 0.11$; and $\alpha'_P = 0.06 \text{ GeV}^{-2}$. We refer to this as KMR2C.

The predictions of the above models and GLM are given in Table 4.

4.5. *Survival probability of the large rapidity gaps (Ref.⁵⁸)*

The calculation of the survival probability for the hard processes is an excellent example to show that the cross section of hard processes cannot be found without knowledge of 'soft' physics. Indeed, hard processes originate from the one parton shower interaction. In order to select this process, it is necessary to apply an additional suppression, so that the interaction of more than one parton shower does not take place. Only in a restricted numbers of cases, when we have inclusive production, do these contributions cancel, and not lead to a suppression. This suppression factor (survival probability) was introduced in Refs.^{76,77} and its general form is:

$$\langle |S^2| \rangle = \frac{\int d^2 b_1 d^2 b_2 \left\{ \sum_{i,k} \langle p|i \rangle^2 \langle p|k \rangle^2 e^{-\frac{1}{2}\Omega_{i,k}((s,(\mathbf{b}_1+\mathbf{b}_2)^2)} S_{i,k}^H(b, b_1, b_2) \right\}^2}{\int d^2 b_1 d^2 b_2 \left\{ \sum_{i,k} \langle p|i \rangle^2 \langle p|k \rangle^2 A_H^i(s, b_1) A_H^k(s, b_2) \right\}^2}, \quad (4.72)$$

where, $\langle p|i \rangle$ is equal to $\langle \Psi_{proton} | \Psi_i \rangle$ and , therefore, $\langle p|1 \rangle = \alpha$ and $\langle p|2 \rangle = \beta$. The factors $\exp[-\Omega_{i,k}/2]$ are responsible for the Good-Walker mechanism contribution to the survival probability, while the factors $S_{i,k}^H(b, b_1, b_2)$ take

Table 4. Comparison of results of the different models for $W = 1.8, 7$ and 14 TeV

$W = 1.8$ TeV	GLM	KMR3C	KMR2C	Ostap(C)	BMR*	KP
$\sigma_{\text{tot}}(mb)$	79.2	79.3	77.2	73.0	81.03	75.0
$\sigma_{\text{el}}(mb)$	18.5	17.9	17.4	16.8	19.97	16.5
$\sigma_{SD}(mb)$	11.27	5.9(LM)	2.82(LM)	9.2	10.22	10.1
$\sigma_{DD}(mb)$	5.51	0.7(LM)	0.14(LM)	5.2	7.67	5.8
$B_{\text{el}}(GeV^{-2})$	17.4	18.0	17.5	17.8		
$W = 7$ TeV	GLM	KMR3C	KMR2C	Ostap(C)	BMR*	KP
$\sigma_{\text{tot}}(mb)$	98.6	97.4	96.4	93.3	98.3	96.4
$\sigma_{\text{el}}(mb)$	24.6	23.8	24.0	23.6	27.2	24.8
$\sigma_{SD}(mb)$	14.88	7.3(LM)	3.05(LM)	10.3	10.91	12.9
$\sigma_{DD}(mb)$	7.45	0.9(LM)	0.14(LM)	6.5	8.82	6.1
$B_{\text{el}}(GeV^{-2})$	20.2	20.3	19.8	19.0		
$W = 14$ TeV	GLM	KMR3C	KMR2C	Ostap(C)	BMR	KP
$\sigma_{\text{tot}}(mb)$	109.0	107.5	108.	105.	109.5	108.
$\sigma_{\text{el}}(mb)$	27.9	27.2	27.9	28.2	32.1	29.5
$\sigma_{SD}(mb)$	17.41	8.1(LM)	3.15(LM)	11.0	11.26	14.3
$\sigma_{DD}(mb)$	8.38	1.1(LM)	0.14(LM)	7.1	9.47	6.4
$B_{\text{el}}(GeV^{-2})$	21.6	21.6	21.1	21.4		

into account an additional suppression due to the structure of $\Omega_{i,k}$ (see Fig. 16 for different contributions to $S_{i,k}^H$). Recall that the amplitudes $A_{i,k}$ of Eq. (4.55) are equal to $A_{i,k} = i(1 - \exp(-\frac{1}{2}\Omega_{i,k}))$. A_H^i is the hard process amplitude. Its contribution is critical in the production of the Higgs boson, in a one parton shower.

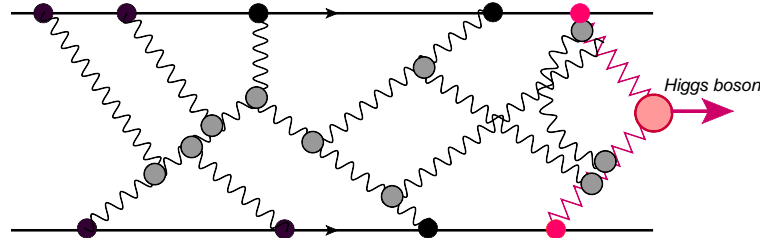


Fig. 16. MPSI approximation: diagrams contributing to the survival probability. Wavy lines denote the BFKL Pomeron, the blob stands for the triple BFKL Pomeron vertex. Zigzag line denote the hard amplitude

$S_{i,k}^H$ can be expressed through the functions \tilde{G} , in the following way:

$$S^H(Y, b) = \int d^2 b_1 \frac{A_i^H(\vec{b} - \vec{b}_1)}{\left(1 + \tilde{g}_k(\vec{b} - \vec{b}_1) T(Y) + \tilde{g}_i(b_1) T(Y/2 - y_h/2)\right)} \times \frac{A_k^H(b_1)}{\left(1 + \tilde{g}_i(\vec{b} - \vec{b}_1) T(Y) + \tilde{g}_k(b_1) T(Y/2 + y_h/2)\right)}. \quad (4.73)$$

$y_h = \ln(M_{Higgs}^2/s_0)$ with $s_0 = 1 \text{ GeV}^2$.

Substituting in Eq. (4.72) for specific values of M at the relevant energy, we obtain values of the SP which are plotted in Fig. 17.

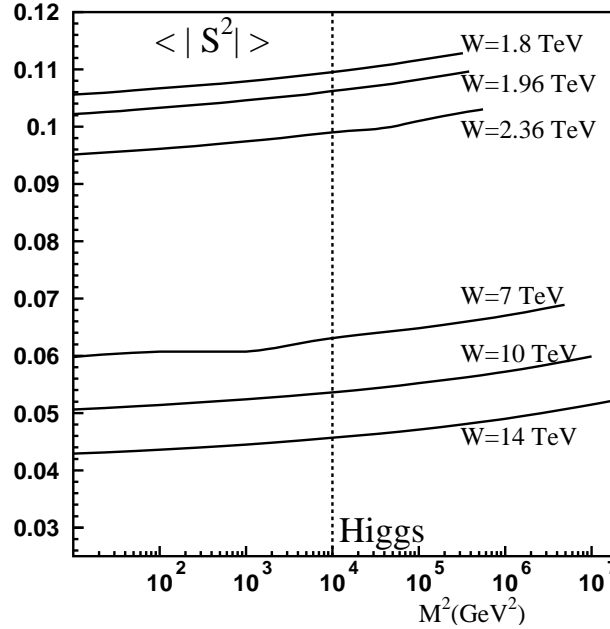


Fig. 17. The estimates for the value of SP for dijets with mass M . The scale on the y axis denotes the value of $\langle |S^2| \rangle$. The dotted line corresponds to the Higgs boson production with $M_{Higgs} = 100 \text{ GeV}$. We estimate a $60 \div 70\%$ margin of error in our results.

Based on the errors assigned to our fitted parameters, we estimate the margin of errors of our results to range from 60% at $W=2 \text{ TeV}$ to 70% at $W=14 \text{ TeV}$. The central values obtained are shown in Fig. 17. The margin of error in our results were estimated by the uncertainty present in our parametrization of the hard amplitude (see⁵¹ and Eq. (4.72)), e.g. the slope and coupling of the elastic and inelastic hard amplitudes were taken from the HERA data for J/Ψ production,⁷³ where $4 \leq B_{el}^H = R_H^2/2 \leq 6 \text{ GeV}^{-2}$, and $0.5 \leq B_{inel}^H \leq 1.5 \text{ GeV}^{-2}$. Our esti-

Table 5. Comparison of values obtained by GLM⁵⁸ and KMR.⁷² KMR present four models, the numbers quoted are those of their "favoured" model 4.

W (TeV)	GLM (%)	KMR2 (%)
1.8	7.02	2.8
7	2.98	1.5
14	1.75	1.0

mates are compatible with the CDF Tevatron data³⁵ as well as with the theoretical estimates.^{74,75}

Our values of SP and its mild dependence of the mass of produced di-jets have the same origin, the small values of G_{3P} .

Our main conclusions are that the value of the SP, as well as its mass dependence are very sensitive to both the particular form adopted for the Pomeron interaction, and to the values of the fitted parameters that determine the strength of the contribution of the enhanced diagrams.

4.5.1. Inclusive cross sections(Ref.⁷⁹)

In the framework of Pomeron calculus, single inclusive cross sections can be calculated using the Mueller diagrams⁸³ shown in Fig. 18-a. They lead to

$$\begin{aligned} \frac{1}{\sigma_{in}} \frac{d\sigma}{dy} = \frac{1}{\sigma_{in}(Y)} & \left\{ a_{PP}(\alpha^2 g_1 + \beta^2 g_2)^2 G_{enh}(T(Y/2 - y)) \times G(T(Y/2 + y)) \right. \\ & - a_{RP}(\alpha^2 g_1^R + \beta^2 g_2^R)(\alpha^2 g_1 + \beta^2 g_2) \\ & \left. \left[e^{(\Delta_R(Y/2 - y))} \times G(T(Y/2 + y)) + e^{(\Delta_R(Y/2 - y))} \times G(T(Y/2 + y)) \right] \right\}, \end{aligned} \quad (4.74)$$

where, $G(T)$ is given by Eq. (3.40) and sums all enhanced diagrams of Fig. 18-b. We need to replace

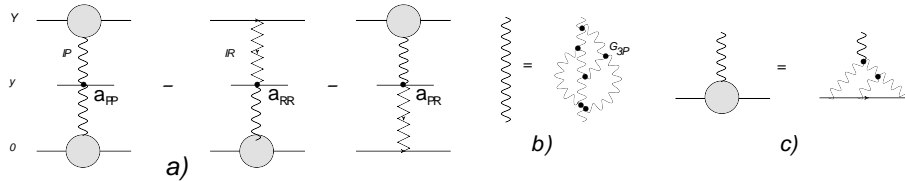


Fig. 18. Mueller diagrams⁸³ for a single inclusive cross section. A bold wavy line presents the exact Pomeron Green function of Eq. (3.40), which is the sum of the enhanced diagrams of Fig. 18-b. A zig-zag line corresponds to the exchange of a Reggeon. Fig. 18-c is a graphic form presenting the vertex that includes the Pomeron interaction (see Eq. (4.75).

$$g_i(b) \rightarrow \Gamma_i(y, b) = \frac{g_i S_i(b)}{1 + g_i G(y) S_i(b)}, \quad (4.75)$$

Table 6. Values of parameters used for the two fits.

Data	a_{PP}	a_{PR}	Q_0/Q
CMS	0.39	0.186	0.427
All	0.413	0.194	0.356

so as to take into account the fan diagrams shown in Fig. 18-c.

This calculation entails three additional parameters. The determination of these parameters from existing data¹² is not trivial. Comparing the numbers corresponding to the data shown in Fig. 19, it is evident that a conventional overall χ^2 analysis is impractical, owing to the quoted error bars of the 546 GeV data points, which are considerably smaller than the error bars quoted for the other energies. The full lines in Fig. 19 are the results derived from a χ^2 fit to the 200-1800 GeV data, excluding the 546 GeV points. This fit yields a seemingly poor $\chi^2/d.o.f = 3.2$. Despite this, we consider this fit to be acceptable, as the data points "oscillate" about a uniform line with error bars which are much smaller than their deviation from a smooth average. In our procedure, the line for 546 GeV in Fig. 19 is calculated with the model parameters and is visually compatible with the experimental data points. Note that both the axes of Fig. 19 are linear, and that our calculation coincides with the LHC experimental results¹ and.³ We have also made predictions for the higher energies at which the LHC is expected to run, see Fig. 19. The contributions of the secondary Regge trajectories are minimal. The experimental values for $\sigma_{in} = \sigma_{tot} - \sigma_{el} - \sigma_{diff}$ were taken from Refs.^{1,3,12} For our predictions we have used the values of σ_{in} calculated in our GLMM model. Our output over-estimates the few data points with $\eta > 4$ data at 546 and 900 GeV by up to 20%. This is to be expected, as we have not taken into account the parton correlations due to energy conservation, which are important in the fragmentation region, but difficult to include in the framework of Pomeron calculus.

We extract the three new parameters: a_{PP} , a_{PR} and Q_0/Q from the experimental inclusive data. a_{PP} and a_{PR} describe the emission of hadrons from the Pomeron and the Reggeon. As well as two dimensional parameters Q and Q_0 , Q is the average transverse momentum of produced minijets, and $\frac{Q_0}{2}$ denotes the mass of the slowest hadron produced in the decay of the minijet (see Ref.⁸¹ for more details).

We made two separate fits: (a) fitting only the CMS data at different LHC energies (see Fig. 19-a); and (b) fitting all inclusive data for $W \geq 546 \text{ GeV}$ (see Fig. 19-b). We choose only data in the central region of rapidity, as we have not included energy conservation, and therefore our model is inadequate to describe the data behavior in the fragmentation region. Fig. 19 shows that the soft model based on the Pomeron approach is able to describe the behavior and the value of the inclusive production observed experimentally. Our predictions are shown in the same figure. We note that the final version of our approach which includes the contributions of enhanced, semi-enhanced and net diagrams (see Ref.⁷⁸) provides a

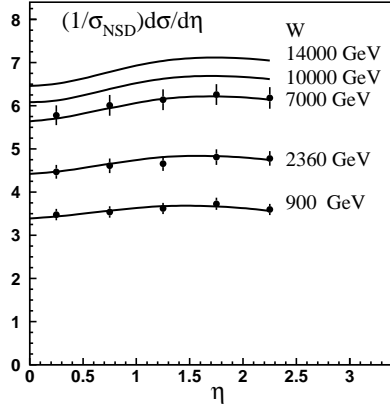


Fig. 19-a

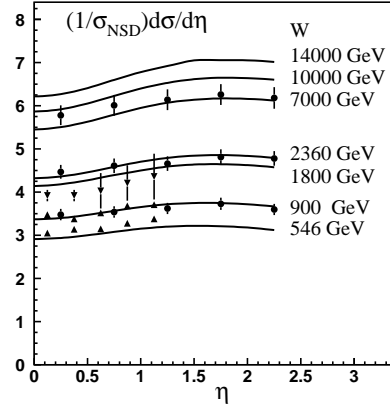


Fig. 19-b

Fig. 19. The single inclusive density versus energy. The data were taken from Refs.¹⁻³ and from Ref.¹² The fit to the CMS data is plotted in Fig. 19-a, while Fig. 19-b presents the description of all inclusive spectra with $W \geq 546 \text{ GeV}$.

much better description of the data than we obtained in our previous attempt,⁷⁹ where only enhanced diagrams were summed.

4.5.2. Double inclusive production: two particle correlations)(Ref.⁸⁴)

In this section we take the next step (following the successful description of inclusive hadron production) in describing the structure of the bias events without the aid of Monte Carlo codes. Two new results are presented : (i) a method for calculating the two particle correlation functions in the BFKL Pomeron calculus in zero transverse dimension; and (ii) an estimation of the values of these correlations in a model of soft interactions.

The Mueller diagrams⁸³ that contribute to double inclusive cross section are shown in Fig. 20.

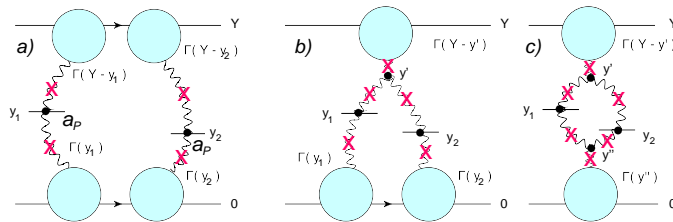


Fig. 20. Mueller diagrams for double inclusive production . Crosses mark the cut Pomerons. $G(y)$ is given by Eq. (3.40) and Γ_i by Eq. (4.75). All rapidities are in the laboratory reference frame.

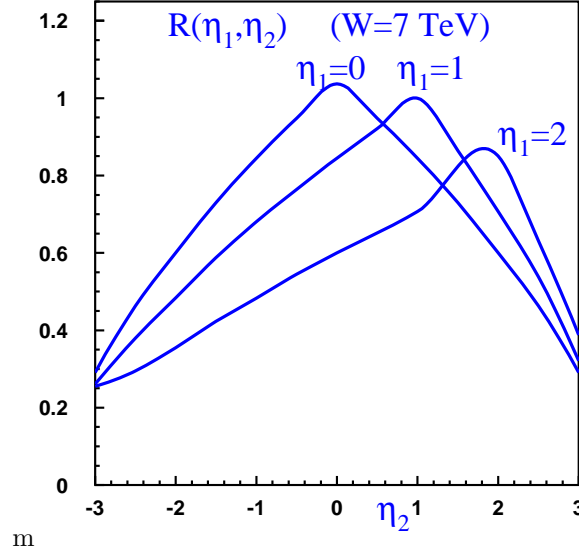


Fig. 21. Multiplicity distribution measured by the CMS collaboration⁸⁵ and our parameters discussed in⁸⁴

All ingredients of Fig. 20 have been discussed above: the Pomeron propagator is given by Eq. (3.40) and $\Gamma_i(Y, b)$ should be taken from Eq. (4.75).

In Pomeron calculus the long range correlations in rapidity stem from the production of two hadrons from two different Pomerons (two different parton showers), as shown in (l.h.) figure. i.e. two hadrons in the central rapidity region can be produced in an event with more than two parton showers.

$$R(y_1, y_2) = \frac{\rho_2(y_1, y_2) - \rho(y_1)\rho(y_2)}{\rho(y_1)\rho(y_2)} = \frac{\frac{1}{\sigma_{in}} \frac{d^2\sigma}{dy_1 dy_2}}{\frac{1}{\sigma_{in}} \frac{d\sigma}{dy_1} \frac{1}{\sigma_{in}} \frac{d\sigma}{dy_2}} - 1.$$

σ_{in} denotes the inelastic cross section $\rho_2(y_1, y_2) = \frac{1}{\sigma_{in}} \frac{d^2\sigma}{dy_1 dy_2}$ and $\rho(y) = \frac{1}{\sigma_{in}} \frac{d\sigma}{dy}$.

If particles were emitted independently then $\rho_2(y_1, y_2) = \rho(y_1)\rho(y_2)$.

Our results for $R(\eta_1, \eta_2)$ versus η_2 at different values of η_1 at $W = 7 \text{ TeV}$ is shown in Fig. 21.

Surprisingly this function falls steeply at large η_2 . This is not expected since all three diagrams which contribute generate long range rapidity correlations. The main contribution comes from the enhanced diagram Fig. 20-c. The eikonal-type diagram of Fig. 20-a leads to long range rapidity correlations which do not depend on the values of η_1 and η_2 . The diagram of Fig. 20-b gives a negligible contribution.

Using parameters determined in our fit to the Single Inclusive Cross Section for $W = 7 \text{ TeV}$ and $|\eta| \leq 0.5$, i.e. $\langle n \rangle = 5.8$ and $r = 1.25$.⁷⁸

40 *E. Gotsman, E. Levin and U. Maor*

Table 7. Normalized Moments $C_q = \langle n^q \rangle / \langle n \rangle^q$ for $W = 7$ TeV and $|\eta| \leq 0.5$.

q	3	4	5
CMS	5.8 ± 0.6	22 ± 2	90 ± 18
GLM	5.65	21.18	98.2

Then

$$\frac{\sigma_n}{\sigma_{in}} = \left(\frac{r}{r + \langle n \rangle} \right)^r \frac{\Gamma(n+r)}{n! \Gamma(r)} \left(\frac{\langle n \rangle}{r + \langle n \rangle} \right)^n.$$

Table 8. $R(y_1 = 0, y_2 = 0)$ for different energies.

W(TeV)	0.9	1.8	2.36	7
$R(y_1 = 0, y_2 = 0)$	1.0	1.12	1.026	1.034

This result is in a good agreement with the CMS data on multiplicity distribution.⁸⁵ Indeed, experimentally, $C_2 = \langle n^2 \rangle / \langle n \rangle^2$ was measured for the rapidity window $|\eta| < 0.5$ in the energy range $W = 0.9$ to 7 TeV (see Fig. 21 in Ref.⁸⁵) and $C_2 \approx 2$. For this small range of rapidity, we can consider that $C_2 = R(0, 0) + 1$. It is worthwhile mentioning that using our calculation of $R(0, 0)$, we can calculate the parameters of the negative binomial distribution. Using this distribution we calculate $C_q = \langle n^q \rangle / \langle n \rangle^q$ given in Table 7.

The attraction of the Pomeron approach reveals itself in the possibility to discuss not only the forward scattering data but, also, to make predictions relating to multiparticle production processes using the AGK cutting rules.⁸²

4.5.3. Proton-Air scattering (Ref.⁸⁶)

As we have discussed above, the LHC data¹⁻⁴ provided two important lessons for our understanding of soft interactions at high energy. The first, regrettably, none of the phenomenological models based on the Reggeon approach were able to predict the data, in spite of having a large number of fitting parameters. The second, a more encouraging one, the LHC data could be fitted by choosing a new set of the parameters without changes in the theoretical scheme of the models. The natural question that arises, is whether the new set of parameters has any predictable power, or its life time is only until new measurements at higher energies appear. In particular, we ask this question in relation to our model, and to our final set of fitting parameters (see Table 1). Our model has passed the first check: as one can see from Table 3 it is able to describe the proton-proton inelastic and total cross section at $W = 57$ TeV that has been extracted from the Pierre Auger Collaboration data on

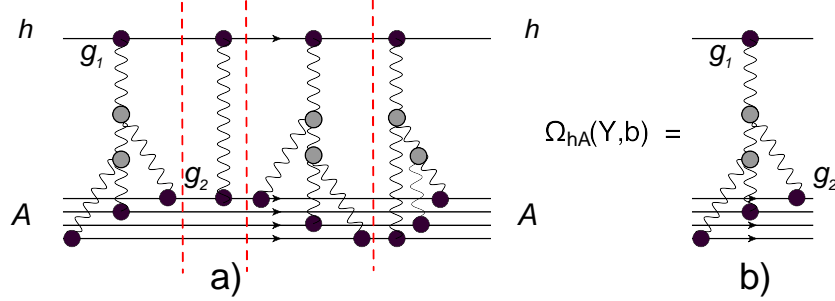


Fig. 22. The set of diagrams that contribute to the scattering amplitude of hadron-nucleus scattering in the kinematic region given by Eq. (4.76). Fig. 22-b shows the hadron-nucleus irreducible diagrams while the general case is shown in Fig. 22-a. The vertical dashed lines indicate the hadron-nucleus states. The wavy lines denote the soft Pomerons.

proton-Air interactions.⁸⁷ Our goal in this section is to compare our model directly with the cosmic ray data on the proton-Air interactions. We re-visit the problem of hadron-nucleus interactions at high energies. It is well known that the Glauber-Gribov approach,^{88,89} where the total cross section of the hadron-nucleus interaction is expressed through the inelastic cross section of hadron-proton scattering, can only be justified at rather low energies, where corrections due to Pomeron interactions may be neglected. A more general approach has been developed^{86,90-92} in which the Pomeron interactions have been taken into account in the energy range for :

$$\begin{aligned} g S_A(b) G_{3P} e^{\Delta_{PY}} &\propto g G_{3P} A^{1/3} e^{\Delta_{PY}} \approx 1; \\ g G_{3P} e^{\Delta_{PY}} &< 1; \quad g G_{3P}^2 e^{\Delta_{PY}} e^{\Delta_{PY}} \ll 1. \end{aligned} \quad (4.76)$$

For the nuclear profile $S_A(b)$ we use the general expression

$$S_A(b) = \int_{-\infty}^{+\infty} dz \rho(z, b) \quad \int d^2b S_A(b) = A; \quad (4.77)$$

where $\rho(z, b)$ is the density of nucleons in a nucleus.

In this region we need to sum the diagrams of Fig. 22. The final formula that includes both the Good-Walker mechanism of low mass diffraction and the enhanced Pomeron diagrams is:

$$\begin{aligned} \sigma_{in}(p + A; Y) &= \int d^2b \left(1 - \exp \left(- \left\{ 2 \operatorname{Im} a_{pp}^{el} \left(Y, \vec{b} - \vec{b}' \right) S_A \left(Y; \vec{b}' \right) \right. \right. \right. \\ &\quad \left. \left. \left. - \left[\sigma_{el} \left(Y, \vec{b} - \vec{b}' \right) + \sigma_{diff} \left(Y, \vec{b} - \vec{b}' \right) \right] \frac{S_A^2 \left(Y; \vec{b}' \right)}{S_A \left(\vec{b}' \right)} \right\} \right) \right); \\ \sigma_{el} \left(Y, \vec{b} - \vec{b}' \right) + \sigma_{diff} \left(Y, \vec{b} - \vec{b}' \right) &= \\ |a_{pp}^{el} \left(Y, \vec{b} - \vec{b}' \right)|^2 + |a_{pp}^{sd} \left(Y, \vec{b} - \vec{b}' \right)|^2 + |a_{pp}^{dd} \left(Y, \vec{b} - \vec{b}' \right)|^2. \end{aligned} \quad (4.78)$$

Before comparing with the experimental results, we would like to draw the reader's attention to the fact that some of the experimental results shown might be overestimated, due to the possibility of the airshowers being created by helium nuclei, as well as protons. The importance of this phenomena has been investigated by Block⁹⁴ and the Auger collaboration.⁸⁷ We refer the reader to these references for further details. In the paper of the Pierre Auger collaboration, a possible contamination of 25% of helium was assumed which produces an uncertainty of about 30 mb (which is less than 10% of their final result), and is included in their systematic error.

The results of our calculations are shown in Fig. 23. For our calculations we used the parameters of our model, presented in Table 1 and Table 2. For the scattering with air we use $S_{\text{Air}}(b) = 0.78S_{\text{Ng}}(b) + 0.22S_{\text{O}}(b)$ where Ng and O denote nitrogen and oxygen, respectively. For both these nuclei we used the harmonic oscillator parametrization, following Ref.⁹⁵

Two conclusions follow from the results of our calculations. First, all formulae including the Glauber-Gribov one, give good agreement with the experimental data. This agreement improves (at least does not deteriorate) at ultra high energies beyond the accelerator region ($W > 8\text{TeV}$).

Second, the inelastic Gribov corrections (Fig. 23 the curve with $G_{3P} = 0$), decrease the value of the inelastic p-Air cross section by 7 - 10% which are within the experimental errors. The corrections due to the Pomeron interaction turns out to be negligibly small (see our model curve in Fig. 23). We would like to stress that our model⁶ gives a smaller contribution for Pomeron interactions, when compared to other attempts to describe the LHC data.^{8,9}

We also calculate the total and inelastic cross sections for proton-lead interaction at high energy, to check whether the corrections due to Pomeron interactions are visible in the collisions with heavy nuclei. For a heavy nucleus such as lead we can use Eq. (3.31), and our prediction will not depend on the details of b distribution for the proton-proton scattering. We employ the Wood-Saxon parametrization for $S_A(b)$

$$S_A(b) = \int_{-\infty}^{\infty} dz \frac{\rho_0}{1 + \exp\left(\frac{\sqrt{z^2 + b^2} - R_A}{h}\right)}. \quad (4.79)$$

Fig. 24 shows our predictions for the total and inelastic cross sections for the proton-lead interaction at high energy. For heavy nuclei the difference between our approach and Glauber-Gribov formula is not large, reaching about 11% for the total and 5% for the inelastic cross sections. It is instructive to note that the inelastic cross section for heavy nuclei is not sensitive to Pomeron interactions, and the major difference from Glauber-Gribov formula stems from Good-Walker mechanism for low mass diffraction in proton-proton collisions. However, all three contributions influence the value and energy behaviour of the total cross sections.

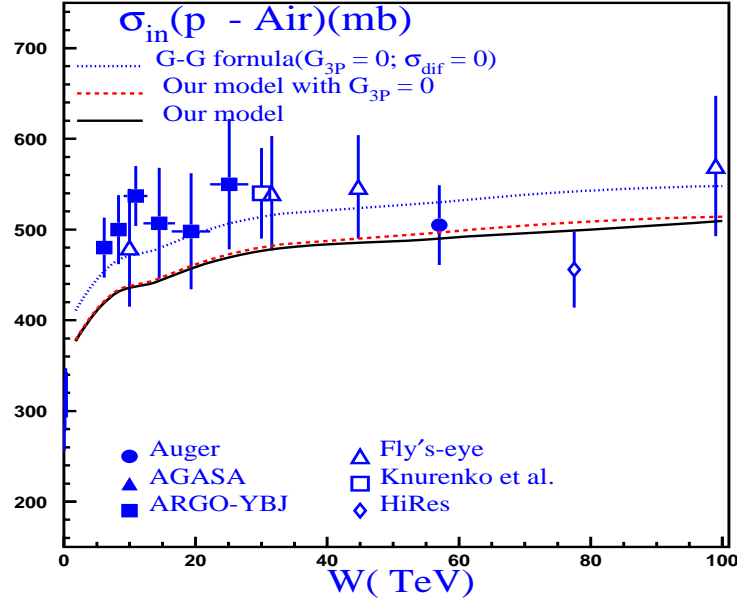


Fig. 23. Comparison the energy dependence of the total cross section for proton-Air interaction with the high energy experimental data. Data are taken from Refs.⁹⁶⁻¹⁰⁰ $p_{lab} = W^2/(2m)$ where m denotes the proton mass.

5. Conclusions

Our model, reviewed here, gives an example of a self consistent approach, that incorporates our theoretical understanding of long distance physics, based both on N=4 SYM for strong coupling and on the matching with the perturbative QCD approach. We hope that we have demonstrated how important and decisive the LHC data are on strong interactions which led us to the set of the phenomenological parameters that fully confirmed our theoretical expectations. We also showed how far we have come towards creating the framework for the description of the minimal bias events for high energy scattering without need to generate Monte Carlo codes.

A result emerging from our rather complex calculations and phenomenology is a simple picture of a hadron, in which a fast hadron is a quantum mixture of two state: the large component leads to gray disc regime with the transparency which is sizeable even at energies as high as $W = 57 TeV$; and the small black component which reaches the unitarity bound at rather low energies. The sizes of these components do not depend on energy while the blackness increases at high energies.

On the qualitative level, this picture is very similar to the structure of the interaction that arises from the saturation/CGC approach (see⁴⁵ and references therein).

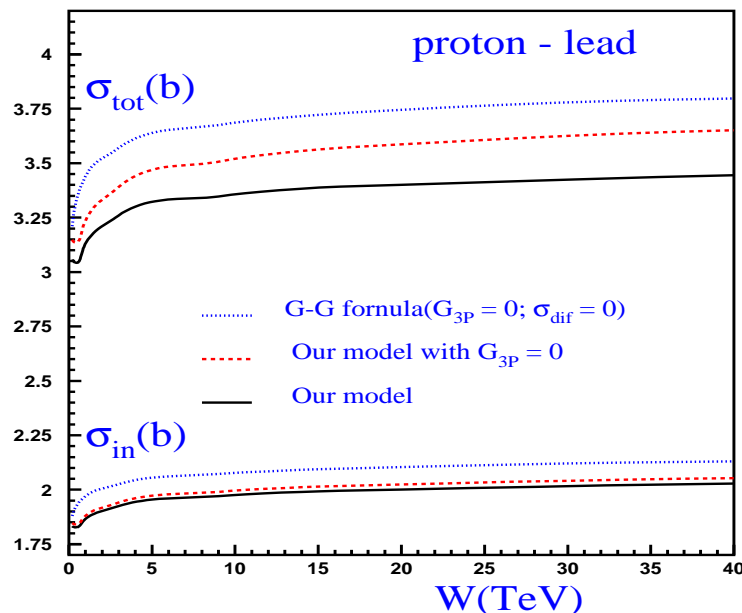


Fig. 24. Our model predictions for proton-lead cross sections. In this figure σ in barns while W in TeV.

Unfortunately, our model does not include a matching with this approach in spite of providing a qualitatively close picture. Some attempts have been made^{101,102} to include the main features of the saturation/CGC approach in the soft interaction models, but they are far from being self consistent approaches, and so we feel it is premature to discuss them.

Lev Landau taught his students: “A model is a theory which has not yet been proven to be correct”. We hope that our model is just an illustration of these words.

6. Acknowledgements

We would like to thank Boris Kopeliovich and Gosta Gustafson for supplying the numerical values of their amplitudes, and Christophe Royon for suggesting that we write this review. The research was supported by the BSF grant 2012124 and by the Fondecyt (Chile) grants 1140842 and 1130549.

References

1. M. G. Poghosyan, J. Phys. G **38**, 124044 (2011) [arXiv:1109.4510 [hep-ex]]. ALICE Collaboration, “First proton–proton collisions at the LHC as observed with the ALICE detector: measurement of the charged particle pseudorapidity density at $\sqrt{s} = 900$ GeV,” arXiv:0911.5430 [hep-ex].

2. G. Aad *et al.* [ATLAS Collaboration], Nature Commun. **2**, 463 (2011) [arXiv:1104.0326 [hep-ex]].
3. CMS Physics Analysis Summary: “Measurement of the inelastic pp cross section at $s = 7$ TeV with the CMS detector”, 2011/08/27.
4. F. Ferro [TOTEM Collaboration], AIP Conf. Proc. **1350**, 172 (2011) ; G. Antchev *et al.* [TOTEM Collaboration], Europhys. Lett. **96**, 21002 (2011), **95**, 41001 (2011) [arXiv:1110.1385 [hep-ex]].
5. A. Donnachie and P.V. Landshoff, Nucl. Phys. **B231**, (1984) 189; Phys. Lett. **B296**, (1992) 227; Zeit. Phys. **C61**, (1994) 139.
6. E. Gotsman, E. Levin and U. Maor, Eur. Phys. J. C **71**, 1553 (2011) [arXiv:1010.5323 [hep-ph]]; E. Gotsman, E. Levin, U. Maor and J. S. Miller, Eur. Phys. J. C **57**, 689 (2008) [arXiv:0805.2799 [hep-ph]].
7. A. B. Kaidalov and M. G. Poghosyan, arXiv:0909.5156 [hep-ph].
8. A. D. Martin, M. G. Ryskin and V. A. Khoze, arXiv:1110.1973 [hep-ph].
9. S. Ostapchenko, Phys. Rev. D **83**, 014018 (2011) [arXiv:1010.1869 [hep-ph]].
10. M. G. Ryskin, A. D. Martin and V. A. Khoze, Eur. Phys. J. C **72** (2012) 1937 [arXiv:1201.6298 [hep-ph]].
11. N. Cartiglia, arXiv:1305.6131 [hep-ex].
12. J. Beringer et al. (Particle Data Group), Phys. Rev. **D86**, 010001 (2012)
13. Ralph Blumenhagen, Dieter Lüst and Stefan Theisen, “*Basic concepts of string theory*”, theoretical and mathematical physics, Springer-Heidelberg New York Dordrecht London, 2013. J. Polchinski, “*String Theory*”, Monographs on mathematical physics, University Press, Cambridge, 1998.
14. E. A. Kuraev, L. N. Lipatov, and F. S. Fadin, Sov. Phys. JETP **45**, 199 (1977); Ya. Ya. Balitsky and L. N. Lipatov, Sov. J. Nucl. Phys. **28**, 22 (1978).
15. L. N. Lipatov, Phys. Rep. **286** (1997) 131; Sov. Phys. JETP **63** (1986) 904 and references therein.
16. J. M. Maldacena, Adv. Theor. Math. Phys. **2** (1998) 231 [Int. J. Theor. Phys. **38** (1999) 1113] [arXiv:hep-th/9711200]; S. S. Gubser, I. R. Klebanov and A. M. Polyakov, Phys. Lett. B **428** (1998) 105 [arXiv:hep-th/9802109]; E. Witten, Adv. Theor. Math. Phys. **2** (1998) 505 [arXiv:hep-th/9803131].
17. J. Polchinski and M. J. Strassler, JHEP **0305** (2003) 012 [arXiv:hep-th/0209211]; Phys. Rev. Lett. **88** (2002) 031601 [arXiv:hep-th/0109174].
18. A. V. Kotikov, L. N. Lipatov, A. I. Onishchenko and V. N. Velizhanin, Phys. Lett. B **595** (2004) 521 [Erratum-ibid. B **632** (2006) 754] [arXiv:hep-th/0404092]; A. V. Kotikov and L. N. Lipatov, Nucl. Phys. B **661** (2003) 19 [Erratum-ibid. B **685** (2004) 405] [arXiv:hep-ph/0208220]; A. V. Kotikov and L. N. Lipatov, Nucl. Phys. B **582** (2000) 19 [arXiv:hep-ph/0004008].
19. R. C. Brower, J. Polchinski, M. J. Strassler and C. I. Tan, JHEP **0712** (2007) 005 [arXiv:hep-th/0603115]; R. C. Brower, M. J. Strassler and C. I. Tan, JHEP **0903** (2009) 092 [arXiv:0710.4378 [hep-th]]; JHEP **0903** (2009) 050. [arXiv:0707.2408 [hep-th]].
20. M. Froissart, Phys. Rev. **123** (1961) 1053; A. Martin, “*Scattering Theory: Unitarity, Analyticity and Crossing.*” Lecture Notes in Physics, Springer-Verlag, Berlin-Heidelberg-New-York, 1969.
21. E. L. Feinberg and I. Pomeranchuk, Nuovo Cimento Suppl. **3** (1956) 652.
22. M. L. Good and W. D. Walker, Phys. Rev. **120** (1960) 1857.
23. P.D.B. Collins, “*An introduction to Regge theory and high energy physics*”, Cambridge University Press 1977.
24. Luca Caneschi (editor), “*Regge Theory of Low $-p_T$ Hadronic Interaction*”, North-

46 *E. Gotsman, E. Levin and U. Maor*

- Holland 1989.
25. E. Levin, "An introduction to Pomerons", arXiv:hep-ph/9808486; "Everything about Reggeons. I: Reggeons in *soft* interaction", arXiv:hep-ph/9710546.
 26. R. P. Feynman, *Phys. Rev. Lett.* **23** (1969) 1415; "Photon-Hadron Interactions", Reading 1972, p282
 27. V. N. Gribov, "Space-time description of hadron interactions at high energies", arXiv:hep-ph/0006158 (2000).
 28. V. N. Gribov, *Sov. J. Nucl. Phys.* **9** (1969) 369 [*Yad. Fiz.* **9** (1969) 640].
 29. G. Gustafson, *Phys. Lett. B* **718**, 1054 (2013) [arXiv:1206.1733 [hep-ph]].
 30. V. N. Gribov, *Sov. Phys. JETP* **26** (1967) 414 [*Zh. Eksp. Teor. Fiz.* **53** (1967) 654].
 31. P. Grassberger and K. Sundermeyer, *Phys. Lett.* **B77** (1978) 220. E. Levin, *Phys. Rev.* **D49** (1994) 4469.
 32. K. G. Boreskov, "Probabilistic model of Reggeon field theory", arXiv:hep-ph/0112325 and reference therein.
 33. F. E. Low, *Phys. Rev.* **D12** (1975) 163. S. Nussinov, *Phys. Rev. Lett.* **34** (1975) 1286.
 34. T. Altinoluk, A. Kovner, E. Levin and M. Lublinsky, "Reggeon Field Theory for Large Pomeron Loops," arXiv:1401.7431 [hep-ph].
 35. F. Abe et al. [CDF Collaboration], *Phys. Rev.* **D50** (1994) 5550.
 36. N. N. Amos et.al.[E710 Collaboration], *Phs. Rev. Lett.* **68** (1992) 2433.
 37. Y. Hatta, E. Iancu and A. H. Mueller, *JHEP* **0801** (2008) 026 [arXiv:0710.2148 [hep-th]].
 38. L. Cornalba and M. S. Costa, *Phys. Rev. D* **78**, (2008) 09010, arXiv:0804.1562 [hep-ph]; L. Cornalba, M. S. Costa and J. Penedones, *JHEP* **0806** (2008) 048 [arXiv:0801.3002 [hep-th]].
 39. B. Pire, C. Roiesnel, L. Szymanowski and S. Wallon, *Phys. Lett. B* **670**, 84 (2008) [arXiv:0805.4346 [hep-ph]].
 40. E. Levin, J. Miller, B. Z. Kopeliovich and I. Schmidt, *JHEP* **0902**, 048 (2009) [arXiv:0811.3586 [hep-ph]].
 41. M. A. Braun, *Phys. Lett.* **B632** (2006) 297 [arXiv:hep-ph/0512057]; *Eur. Phys. J.* **C16** (2000) 337 [arXiv:hep-ph/0001268]; *Phys. Lett.* **B483** (2000) 115 [arXiv:hep-ph/0003004]; *Eur. Phys. J.* **C33** (2004) 113 [arXiv:hep-ph/0309293]; **C6**, 321 (1999) [arXiv:hep-ph/9706373]. M. A. Braun and G. P. Vacca, *Eur. Phys. J.* **C6** (1999) 147 [arXiv:hep-ph/9711486].
 42. E. Levin and I. Potashnikova, *JHEP* **1008** (2010) 112; [arXiv:1007.0306 [hep-ph]].
 43. J. Bartels, M. Braun and G. P. Vacca, *Eur. Phys. J.* **C40** (2005) 419 [arXiv:hep-ph/0412218]. J. Bartels and C. Ewerz, *JHEP* **9909** 026 (1999) [arXiv:hep-ph/9908454]. J. Bartels and M. Wusthoff, *Z. Phys.* **C6**, (1995) 157. A. H. Mueller and B. Patel, *Nucl. Phys.* **B425** (1994) 471 [arXiv:hep-ph/9403256]. J. Bartels, *Z. Phys.* **C60** (1993) 471.
 44. D. Amati, M. Le Bellac, G. Marchesini and M. Ciafaloni, *Nucl. Phys.* **B112** (1976) 107; D. Amati, G. Marchesini, M. Ciafaloni and G. Parisi, *Nucl. Phys.* **B114** (1976) 483.
 45. M. Kozlov and E. Levin, *Nucl. Phys. A* **A779** (2006) 142 [arXiv:hep-ph/0604039]
 46. S. Bondarenko, L. Motyka, A. H. Mueller, A. I. Shoshi and B. -W. Xiao, *Eur. Phys. J. C* **50**, 593 (2007) [hep-ph/0609213].
 47. I. Gradshteyn and I. Ryzhik, *Table of Integrals, Series, and Products*, Fifth Edition, Academic Press, London, 1994.
 48. A. H. Mueller and B. Patel, *Nucl. Phys.* **B425** (1994) 471. A. H. Mueller and G. P. Salam, *Nucl. Phys.* **B475**, (1996) 293. [arXiv:hep-ph/9605302]. G. P. Salam, *Nucl. Phys.* **B461** (1996) 512; E. Iancu and A. H. Mueller, *Nucl. Phys.* **A730** (2004) 460

- [arXiv:hep-ph/0308315]; 494 [arXiv:hep-ph/0309276].
49. E. Levin and A. Prygarin, Eur. Phys. J. **C53** (2008) 385, [arXiv:hep-ph/0701178].
 50. E. Levin, J. Miller and A. Prygarin, Nucl. Phys. **A806** (2008) 245, [arXiv:0706.2944 [hep-ph]].
 51. E. Gotsman, E. Levin, U. Maor and J. S. Miller, Eur. Phys. J. **C57** (2008) 689 [arXiv:0805.2799 [hep-ph]].
 52. A. H. Mueller, Nucl. Phys. **B415** (1994) 373; **B437** (1995) 107.
 53. E. Laenen and E. Levin, Nucl. Phys. **B451** (1995) 207.
 54. E. Levin and M. Lublinsky, Nucl. Phys. A **763** (2005) 172 [arXiv:hep-ph/0501173]; Phys. Lett. B **607** (2005) 131 [arXiv:hep-ph/0411121]; Nucl. Phys. A **730** (2004) 191 [arXiv:hep-ph/0308279].
 55. E. Gotsman, E. Levin and U. Maor, Eur. Phys. J. C **71**, 1553 (2011) [arXiv:1010.5323 [hep-ph]].
 56. K. G. Boreskov, A. B. Kaidalov, V. A. Khoze, A. D. Martin and M. G. Ryskin, Eur. Phys. J. **C44** (2005) 523 [arXiv:hep-ph/0506211].
 57. Y. V. Kovchegov and E. Levin, Nucl. Phys. **B577** (2000) 221 [arXiv:hep-ph/9911523].
 58. E. Gotsman, E. Levin and U. Maor, Eur. Phys. J. C **71**, 1685 (2011) [arXiv:1101.5816 [hep-ph]]; E. Gotsman, E. Levin, U. Maor and J. S. Miller, Eur. Phys. J. C **57**, 689 (2008) [arXiv:0805.2799 [hep-ph]].
 59. J. Pumplin, Phys.Rev. **D 8** 2899 (1973).
 60. H. Miettinen and Jon Pumplin Phys.Rev. **D18**, 1696 (1978).
 61. S. Nussinov, "Is the Froissart bound relevant for the total pp cross section at $s = (14\text{ TeV})^2$?", arXiv:0805.1540 [hep-ph].
 62. Risto Orava of the TOTEM Collaboration (private communication).
 63. V.A. Khoze, A. D. Martin and M.G. Ryskin, arXiv:1402.2778 [hep-ph]
 64. B.Z. Kopeliovich, I.K. Potoshnikova, B. Povh and Ivan Schmidt, *Phys.Rev.* **D76**, 044020 (2007)
 65. E. Ferreira,T. Kodama and A.K. Kohara *Eur. Phys. J.* **C73**, 2326 (2013)
 66. C. Flensburg and G. Gustafson *JHEP* **1010**, 014 (2010)
 67. A.B. Kaidalov and M.G. Poghosyan "Description of soft diffraction in the framework of reggeon calculus: Predictions for LHC", arXiv:[hep-ph] 0909.5156
 68. Ostapchenko S *Phys. Rev.* **D81**, 114028, (2010)
 69. M.G. Ryskin, A.D. Martin and V.A. Khoze *Eur. Phys. J.* **C71**, 1617, (2011)
 70. V.A. Khoze, A. D. Martin and M.G. Ryskin, *Eur.Phys.J.* **C72**, 1937 (2012).
 71. R. Ciesielski and K. Goulianos, "MBR Monte Carlo Simulation in PYTHIA8", arXiv: 1205.1446 [hep-ph]
 72. V.A. Khoze, A. D. Martin and M.G. Ryskin, arXiv: 1306.2149 [hep-ph]
 73. H. Kowalski and D. Teaney, *Phys.Rev.* **D68**, 114005 (2003)
 74. V. A. Khoze, A. D. Martin and M. G. Ryskin, arXiv:[hep-ph] 0705.2314
 75. C. Royon, R. Staszewski,A. Dechambre and O. Kapka, arXiv:1008.0255 [hep-ph], O. Kepka and C. Royon, *Phys. Rev. D* **76**, 034012 (2007).
 76. J.D. Bjorken, *Phys.Rev.* **D47** (1993) 101.
 77. Yuri L. Dokshitzer, Valery A. Khoze, T. Sjostrand, *Phys.Lett.* B274 (1992) 116.
 78. E. Gotsman, E. Levin and U. Maor, *Phys. Rev. D* **84**, 051502 (2011) [arXiv:1103.4509 [hep-ph]].
 79. E. Gotsman, E. Levin and U. Maor, *Phys. Rev. D* **81**, 051501 (2010) [arXiv:1001.5157 [hep-ph]].
 80. E. Gotsman, E. Levin and U. Maor, *Phys. Let. B* **716**, 425 (2012) [arXiv:1208.0898 [hep-ph]].
 81. D. Kharzeev and E. Levin, *Phys. Lett. B* **523**, 79 (2001) [nucl-th/0108006].

48 *E. Gotsman, E. Levin and U. Maor*

82. V. A. Abramovsky, V. N. Gribov and O. V. Kancheli, *Yad. Fiz.* **18**, 595 (1973) [*Sov. J. Nucl. Phys.* **18**, 308 (1974)].
83. A.H. Mueller, *Phys. Rev.* **D2** (1970) 2963.
84. E. Gotsman, E. Levin and U. Maor, *Eur. Phys. J. C* **73** (2013) 2658 [arXiv:1307.4925 [hep-ph]].
85. V. Khachatryan *et al.* [CMS Collaboration], *JHEP* **1101**, 079 (2011) [arXiv:1011.5531 [hep-ex]].
86. E. Gotsman, E. Levin and U. Maor, *Phys. Rev. D* **88** (2013) 114027 [arXiv:1308.6660 [hep-ph]].
87. P. Abreu *et al.* [Pierre Auger Collaboration], *Phys. Rev. Lett.* **109**, 062002 (2012) [arXiv:1208.1520 [hep-ex]].
88. R.J. Glauber, "*Lectures in Theoretical Physics*", edited by W. E. Britten et al. (Interscience, New York) **1**, 315 (1959).
89. V.N. Gribov, *Sov. Phys. JETP* **29** 483 [*Zh. Eksp. Teor. Fiz.* **56** 892 (1969)]; *Sov. Phys. JETP* **30** 709 [*Zh. Eksp. Teor. Fiz.* **57** (1969) 1306].
90. A. Schwimmer, *Nucl. Phys.* **B94**, 445 (1975).
91. A. Kaidalov, *Nucl. Phys. A* **525**, 39 (1991).
92. S. Bondarenko, E. Gotsman, E. Levin and U. Maor, *Nucl. Phys.* **A683**, 649 (2001) [arXiv:hep-ph/0001260].
93. E. Gotsman, A. Kormilitzin, E. Levin and U. Maor, *Nucl. Phys. A* **842**, 82 (2010) [arXiv:0912.4689 [hep-ph]] and references there in.
94. M. M. Block, *Phys. Rev. D* **84**, 09101 (2011) and references therein. [arXiv:1109.2940 [hep-ph]].
95. C. W. De Jagier, H. De Vries, and C. De Vries, *Atomic Data and Nuclear Data Tables*, **Vol.14 No. 5,6**, 479 (1974).
96. K. Belov et al., *Nucl. Phys. B, Proc. Suppl.* **151**, 197 (2006).
97. S. Knurenko et al., *Proceedings of the 26th International Cosmic Ray Conference*, Salt Lake City, 1999 (1999), Vol. 1, p. 372 (unpublished).
98. M. Honda, M. Nagano, S. Tonwar, K. Kasahara, T. Hara, N. Hayashida, Y. Matsumura, M. Teshima, and S. Yoshida, (AGASA) *Phys. Rev. Lett.* **70**, 525 (1993).
99. M. Aglietta et al. (EAS-TOP Collaboration), *Phys. Rev. D* **79**, 032004 (2009).
100. G. Aielli et al. (ARGO Collaboration), *Phys. Rev. D* **80**, 092004 (2009).
101. E. Gotsman, E. Levin and U. Maor, *Phys. Rev. D* **87**, no. 7, 071501 (2013) [arXiv:1302.4524 [hep-ph]].
102. V. A. Khoze, A. D. Martin and M. G. Ryskin, arXiv:1312.3851 [hep-ph].
103. Y. V. Kovchegov and E. Levin, "*Quantum chromodynamics at high energy*," Cambridge monographs on particle physics, nuclear physics and cosmology, 33 Cambridge, UK: Cambridge Univ. Pr. (2012).

